

Modeling and simulation of electrodifusion in dense reconstructions of cerebral tissue

Halvor Herlyng^[0000-0003-2301-9276] and
 Marius Causemann^[0000-0002-8579-2777] and
 Gaute T. Einevoll^[0000-0002-5425-5012] and
 Ada J. Ellingsrud^[0000-0002-8600-578X] and
 Geir Halmes^[0000-0002-4721-1599] and
 Marie E. Rognes^[0000-0002-6872-3710]

Abstract Excitable tissue is fundamental to brain function, yet its study is complicated by extreme morphological complexity and the physiological processes governing its dynamics. Consequently, detailed computational modeling of this tissue represents a formidable task, requiring both efficient numerical methods and robust implementations. Meanwhile, efficient and robust methods for image segmentation and meshing are needed to provide realistic geometries for which numerical solutions are tractable. Here, we present a computational framework that models electrodifusion in excitable cerebral tissue, together with realistic geometries generated from electron microscopy data. To demonstrate a possible application of the framework, we simulate electrodifusive dynamics in cerebral tissue during neuronal activity. Our results and findings highlight the numerical and computational challenges associated with modeling and simulation of electrodifusion and other multiphysics in dense reconstructions of cerebral tissue.

1 Introduction

Our brains are composed of complex cellular tissue consisting of nerve and glial cells, separated by the tortuous extracellular space, and with vasculature running through-

Halvor Herlyng, Marius Causemann, Ada J. Ellingsrud
 Simula Research Laboratory, Kristian Augusts gate 23, 0164 Oslo, Norway, e-mail: hherlyng@simula.no, mariusca@simula.no, ada@simula.no

Marie E. Rognes
 Simula Research Laboratory, Kristian Augusts gate 23, 0164 Oslo, Norway and K. G. Jebsen Centre for Brain Fluid Research, Oslo, Norway e-mail: meg@simula.no

Gaute T. Einevoll
 Norwegian University of Life Sciences, Ås, Norway and University of Oslo, Oslo, Norway e-mail: gaute.einevoll@nmbu.no

Geir Halmes
 Norwegian Artificial Intelligence Research Consortium, Oslo, Norway, e-mail: geir.halmes@nora.ai

out [34]. Brain tissue is excitable: cells communicate through electromagnetic, chemical and mechanical signals, with ion dynamics playing a central role. Signals can be sent directly from cell to cell through synapses via electric potential spikes known as action potentials (APs), while electrochemical changes in the extracellular environment may also excite or inhibit signals.

Understanding the physical mechanisms underlying brain function is key to better understand neurodegenerative and other neurological disorders. A 2024 study estimated that over one third of the global population suffers or has suffered from a neurological condition, such as stroke, epilepsy and dementia [60]. Computational modeling of neuronal biophysics offers a route to improved understanding: models can be tailored to study specific physical mechanisms, such as the response of a cell to an action potential, or how changes in action potential firing frequencies affect ion concentrations in the surrounding cerebral tissue. Moreover, simulations are flexible because the choice of parameters, initial and boundary conditions can often be altered swiftly at low or no cost. However, an inherent modelling challenge is the range of spatiotemporal scales involved in brain biophysics [8, 34]. In space, these processes occur over centimeters at the organ level to sub-nanometers at the atomic level inside cells (Figure 1). In time, processes occurring over seconds and over hours may influence each other.

Traditionally, computational modeling of brain tissue has focused on electrophysiology. An important reason for this is the impressively accurate model of a giant squid axon potential developed by Hodgkin and Huxley in 1952 [28, 26, 15]. Analogies between electrical circuits and neural tissue have resulted in volume conductor theory models, compartmental models and network models, where extra- and intracellular potentials are calculated based on modeling neurons as compartments in a volume conductor or as components of electrical circuits. These models often account for the geometry implicitly, by including homogenized parameters such as volume fractions and tortuosity. Multi-compartmental modeling based on cable theory has developed into the standard framework for mechanistic modeling of neurons [24]. Over the last decades, there has been increasing interest in models accounting for geometry and morphology explicitly [1, 18]. This development has taken place in tandem with modeling cardiac cells and tissue, another example of excitable tissues [65].

While most computational modeling of cerebral tissue has focused on neurons, which are the main signaling units of the nervous system [34], in recent years, glial cells have received an increasing amount of attention [14]. Glial cells constitute at least half of human brain tissue and are now considered to play an important role in cerebral dynamics. For example, the glia known as astrocytes respond to neurotransmitters, partake in modulation and extracellular metabolism of adenosine triphosphate (ATP), and are involved in neuronal signaling pathways through receptor dynamics [21, 39, 10]. Astrocytes also regulate brain function through ion concentrations with examples including potassium buffering [11] and the dynamic role of astrocytic chloride concentrations in volume regulation and cell proliferation [66]. The ion concentrations both in the extracellular and intracellular spaces of the brain play an indispensable role in brain functioning, with up to two orders of magnitude differences between physiological and pathological concentrations [49].

An open question relates to the role of electrodiffusion in brain tissue under physiological and pathological conditions and the coupled response of electric potentials

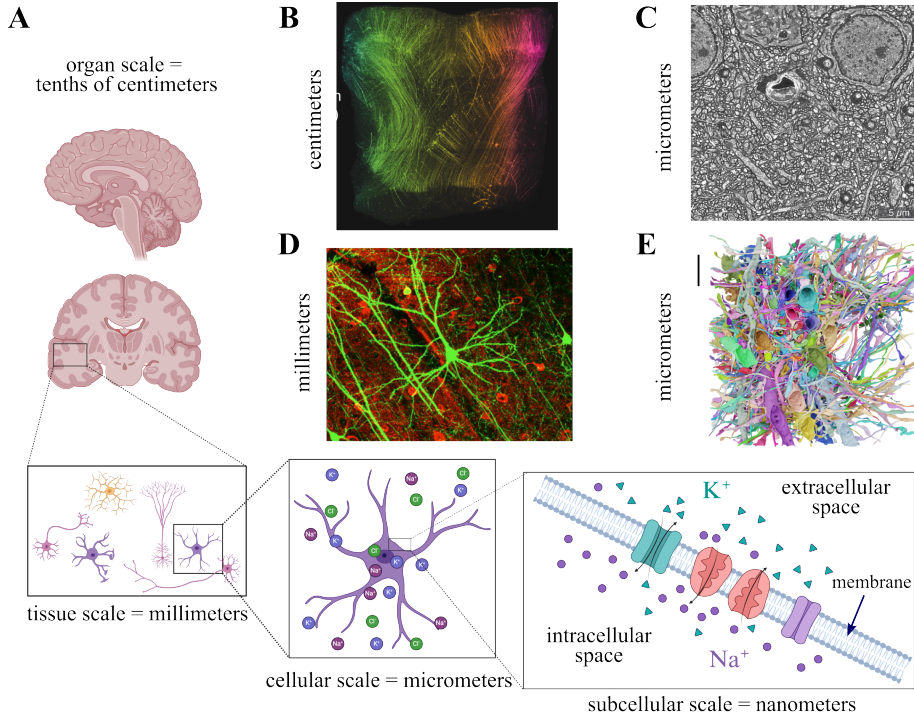


Fig. 1: **A.** The physical scales of the brain, from organ scale to subcellular scale. At the subcellular scale, ions are transported across the cellular membrane through ion channels. The ion channels illustrated on the membrane are, from left to right: open generic ion channel, Na^+/K^+ -ATPase pump importing potassium ions, Na^+/K^+ -ATPase pump exporting sodium ions, and a closed generic ion channel. The illustrations in this panel were created using Biorender. **B.** Plane illumination microscopy of macaque primary motor cortex tissue at centimeter scale [20] **C.** Confocal microscopy image of a neuron (green) in rodent visual cortex tissue. Image spans half a millimeter [38]. **D.** Light-microscopy based reconstructed cross section of mouse hippocampus tissue at the micrometer scale [63]. **E.** 3D rendering of mouse hippocampus tissue, scale bar $3 \mu\text{m}$ [63]. The images in panels **B–E** are reproduced under the terms of the Creative Commons Attribution License.

and ion concentrations. Many electrodiffusion models homogenize or idealize the brain tissue, often considering zero-dimensional cellular compartments or rectangular or cylindrical geometries [25, 58, 54, 55, 56, 57]. These models are particularly suitable for studying the effect of ionic fluxes. For example, Haldnes *et al.* [25] studied a one-dimensional model of an astrocyte coupled with the extracellular space, stimulating the system by adding potassium and removing sodium ions in the astrocyte. Sætra *et al.* [55] used a similar stimulus for an electrodiffusive compartmental model with neuronal, glial and extracellular spaces. There has also been development of electrodiffusive models

that explicitly represent the cellular geometries [43, 48, 41, 18, 40]. These partial differential equation (PDE)-based models are typically solved numerically using finite difference, finite element, or finite volume methods. The explicit geometry representation of individual cells and membranes allows for studying the interplay between cellular shape and function, a key tenet of cellular biology, and for studying spatially varying membrane mechanisms such as distributed ion channels, pumps or cotransporters.

Cell-by-cell models of ionic electrodiffusion are highly demanding to construct and solve computationally [64], for several reasons. First, the morphology of neurons, astrocytes and the extracellular space is highly complex. This makes generation of well-defined, conforming computational meshes challenging in its own right. Moreover, the fine geometric detail calls for high resolution meshes, and the large number of mesh vertices and cells in turn increases computational cost. Second, electrodiffusion involves systems of PDEs with strongly coupled variables, whose dynamics evolve on multiple spatial and temporal scales. Development of efficient and scalable numerical solution algorithms for such coupled problems is an active field of research [51, 5, 16].

Over the last three decades, advances in bioimaging have revolutionized our ability to study the structure and function of living systems. At the nano- to microscale, the new capabilities of cellular microscopy have resulted in the generation and wide availability of large-scale high-resolution imaging data, as strikingly exemplified by increasingly complex dense reconstructions of cortical tissue. Through open distribution of such high-quality imaging data, there now exists several datasets with extremely detailed image data of brain tissue [12]. Together with modern image-processing software and powerful hardware, the image data enables generation of realistic computational geometries of brain tissue. These convergent developments give new opportunities for detailed simulations of spatial ion dynamics in brain tissue.

In this chapter, we present a computational framework for numerically solving ionic electrodiffusion PDEs defined over extremely detailed geometries of mouse visual cortex tissue. We highlight different aspects of the computational pipeline: from the geometric properties of these brain tissue to the numerical properties of the resulting finite element discretization.

2 Dense reconstructions of brain tissue from cell imaging

Brain imaging has been fundamental to our understanding of brain structure and function [71]. Today, the combination of highly detailed cell imaging data and computational processing power allows for a new level of detail in terms of digital representations of brain tissue. Neurons, glial cells and the extracellular space are however characterized by tortuous, meandering structures making meshing of such high-resolution digital reconstructions of brain tissue challenging. One aspect is the computational demand in processing the images, generating surfaces and volumetric meshes. Another key element is that the generated computational mesh must be of sufficient quality for numerical PDE solution algorithms. We here illustrate how these challenges can be addressed by current meshing technology by presenting a pipeline generating conforming tetrahedral meshes from dense image reconstructions.

2.1 From segmented cell imaging to conforming finite element meshes

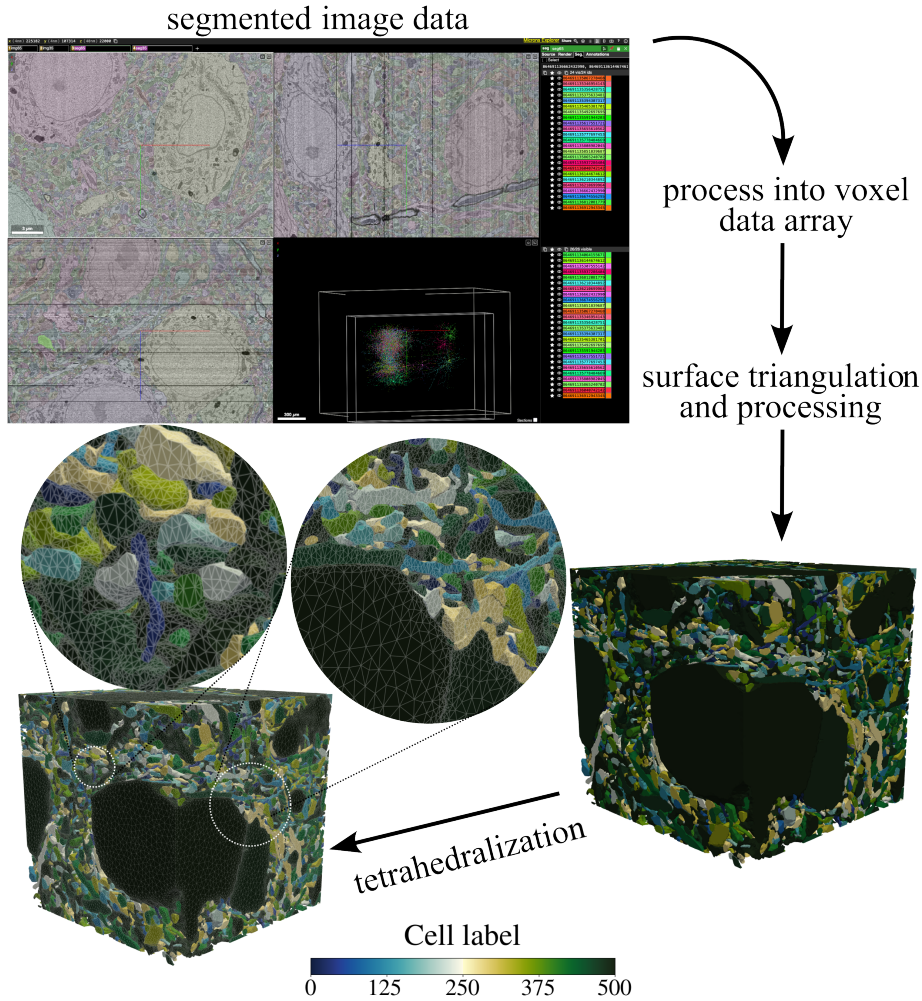


Fig. 2: Illustration of the computational meshing pipeline. Segmented electron microscopy image data, here shown in the MICrONS explorer interface [12], is downloaded and processed into a voxel data array. The voxel data is next converted into triangulated surfaces representing the interfaces between the biological cells and extra-cellular space. These surfaces go through a sequence of morphological processing steps to ensure sufficient mesh quality downstream. Finally, a tetrahedral mesh is generated conforming to the interface surfaces.

The pipeline is implemented in the open-source software EMI-Meshing [9] and consists of the following steps (see also Figure 2):

1. Select and extract segmented image data
2. Filter and/or process the segmentation
3. Construct triangulated surfaces representing the interface between intracellular and extracellular spaces
4. Generate a tetrahedral mesh of the complete volume conforming to the interface surfaces.

First, the raw segmentation data is downloaded at a voxel resolution of $32 \times 32 \times 40$ nm. This data is subsequently resampled to an isotropic resolution of 20 nm. To reduce noise and focus on significant biological structures, we remove small cellular fragments with volumes below 5000 voxels (approximately $0.04 \mu\text{m}^3$) and retain only the N largest biological cells.

We then apply a sequence of morphological operations to process the cellular shapes, utilizing the GPU-accelerated library *pyclesperanto* [22]. All operations are performed with a radius of 1. The cells are first dilated into the background, followed by morphological opening and closing operations which effectively smooth the cellular boundaries. Crucially, all cells are then eroded; this step ensures a physiological volume fraction for the extracellular space and prevents contact between adjacent cells. Following these morphological operations, any remaining disconnected components smaller than the 5000 voxel threshold are removed.

Surface meshes are extracted from the processed voxel data using the marching cubes algorithm implemented in *PyVista* [62]. To ensure computational tractability, the resolution of these surface meshes is reduced by a factor of ten using surface remeshing via the *pyacvd* library [35]. We mitigate staircase artifacts arising from the voxel approximation by applying five iterations of Taubin smoothing in *PyVista*. Next, a cubic surface of edge length L is generated to define the outer boundary of the extracellular space.

Finally, we generate a volumetric mesh of the complete domain, conforming to the triangulated interface surfaces to accurately represent both the intracellular regions and the extracellular space. This step is performed using the *fTetWild* software [29] on the *eX3* high-performance computing infrastructure [37]. The resulting mesh resolution is governed by the *envelope size* and *ideal edge length* parameters. The *envelope size* represents the maximal deviation from the input surface, while the *ideal edge length* defines the target size of the generated tetrahedra. Using a small *envelope size* of 18 nm and a larger *ideal edge length* (1–1.5 % of the bounding box length), the mesh resolution naturally adapts to the shape and morphology of the cellular regions, such that larger intracellular volumes are covered by larger mesh cells than the narrow extracellular space gaps. To ensure element quality suitable for numerical simulation, the mesh is optimized until a maximal conformal AMIPS energy [19] of 10 is reached, thereby eliminating severely distorted tetrahedra. The segmentation labels are transferred from the image data to the volumetric mesh, ensuring that all biological cells and interface surfaces are uniquely labeled in the final computational mesh. These labels or mesh tags facilitate modelling different properties, membrane mechanisms, and initial and boundary conditions for the different biological cells.

We next apply this meshing pipeline to generate computational meshes from the *IARPA MICrONS Cortical mm³* dataset published by the MICrONS consortium [12]. This open dataset includes 3D images spanning a $1.4\text{mm} \times 0.87\text{mm} \times 0.84\text{mm}$ volume of mouse visual cortex obtained using two-photon microscopy, microCT and serial electron microscopy (Figure 2). The image data are already segmented, i.e. each connected component within the 3D image has been identified and assigned a unique label, and can be viewed using the web-visualization tool Neuroglancer [42]. We consider a series of cubical volumes of reconstructed tissue of size $L \times L \times L$ with center point (225182, 107314, 22000) and with $L = 5, 10, 20, 30 \mu\text{m}$. For each of these cubical volumes, we generate a series of computational meshes including the N largest biological cells with $N = 100, 200, 300, 400, 500$ (see Figure 3). The remaining volume is relabeled as extracellular space.

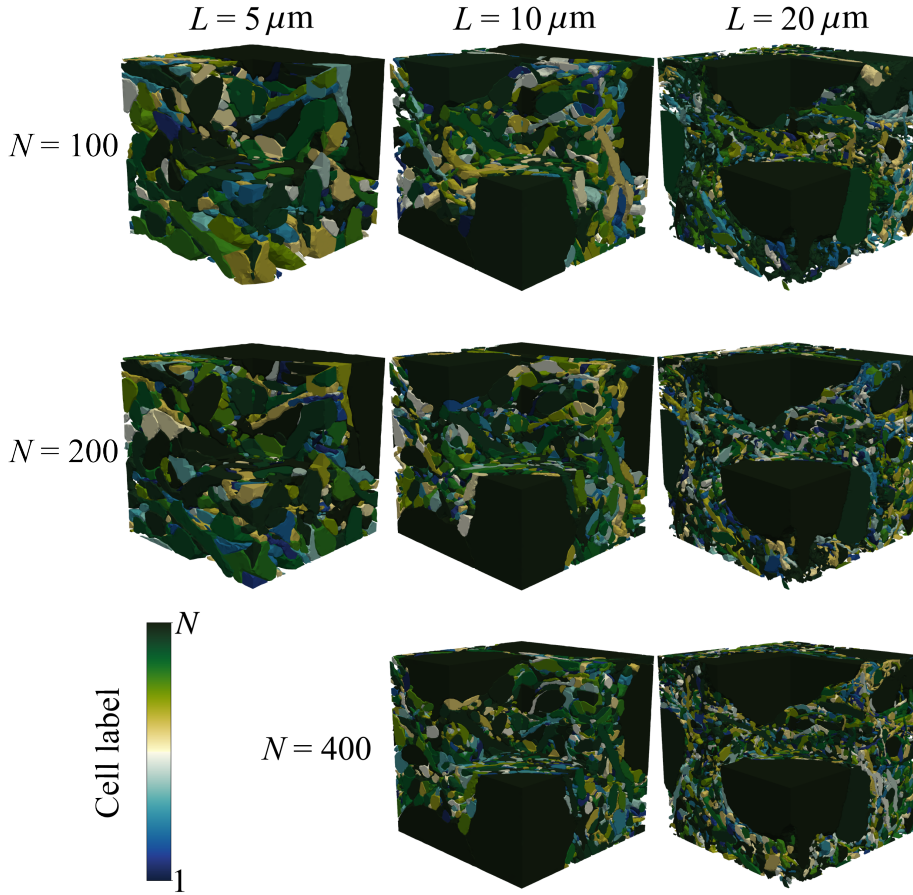


Fig. 3: A sample of the computational meshes generated using the EMI-Meshing pipeline [9] of size $L \times L \times L$ containing N biological cells surrounded by extracellular space.

2.2 Most mesh vertices populate cellular membranes

We next analyze and present quantitative mesh characteristics for the series of cubical meshes of the mouse visual cortex. When including an increasing number of (biological) cells, the general trend for the computational meshes is an increase in the number of computational cells and vertices (Figure 4A, B). However, the increase is not uniform, for instance the number of mesh cells and vertices is lower for the case $N = 400$ than for $N = 300$ when $L = 10$. Notably, the ratio of vertices located on the cell membranes to the total number of vertices generally increases as the meshes become denser. For the largest and densest meshes over 90% of the mesh vertices are on cellular membranes (Figure 4C). Moreover, the volume occupied by the extracellular space is reduced as more biological cells are packed into the geometries (Figure 4D). This also results in a narrower and more tortuous extracellular space. The ECS fraction of the densest meshes are between 17–25%. In real brain tissue, the fraction of extracellular space is commonly reported around 20% [11]. Note that for the mesh with $L = 5 \mu\text{m}$, we only include the $N = 100$ and $N = 200$ meshes, as the maximum number of cells in this cube of tissue with the processing parameters we employ is just shy of 200 cells. For the mesh with size $L = 10 \mu\text{m}$, we further present detailed statistics including the number of ICS and ECS cells, and maximum and minimum edge lengths (Table 1).

Table 1: Statistics for the meshes with size $L = 10 \mu\text{m}$ containing N biological cells ($N = 100, 200, 300, 400, 500$. ICS: intracellular space, ECS: extracellular space.

Quantity	$N = 100$	200	300	400	500
Number of cells	3 292 043	4 489 915	6 693 005	5 625 770	8 061 336
Number of cells in the ICS	1 560 517	2 023 846	2 960 339	2 478 330	3 523 077
Number of cells in the ECS	1 731 526	2 364 127	3 732 666	3 147 440	4 538 259
ECS volume fraction [%]	26.2	20.7	18.4	17.6	17.1
Vertices	574 314	759 501	1 158 188	968 230	1 389 747
Membrane vertices	465 906	661 225	1 073 278	881 889	1 292 304
Membrane vertices fraction [%]	81.1	87.1	92.7	91.1	93.0
Max edge length [nm]	456.1	435.6	449.8	422.6	450.9
Min edge length [nm]	3.6	2.3	5.3	4.5	3.9

3 Modeling electrodiffusion at the cellular scale in explicit geometries

With computational cellular geometries available, we next turn to mathematical modeling of electrodiffusion. In a domain $\Omega \subset \mathbb{R}^3$ representing cerebral tissue, we model ion concentrations $c_k = c_k(\mathbf{x}, t)$ with $k \in K$ for a set of ions $K = \{\text{Na}^+, \text{K}^+, \text{Cl}^-\}$ and the electric potential $\phi = \phi(\mathbf{x}, t)$, for $\mathbf{x} \in \Omega$ and times $t \in [0, T]$. We will for notational brevity drop the valence of the ions in the subscripts k . At the cellular scale, brain tissue

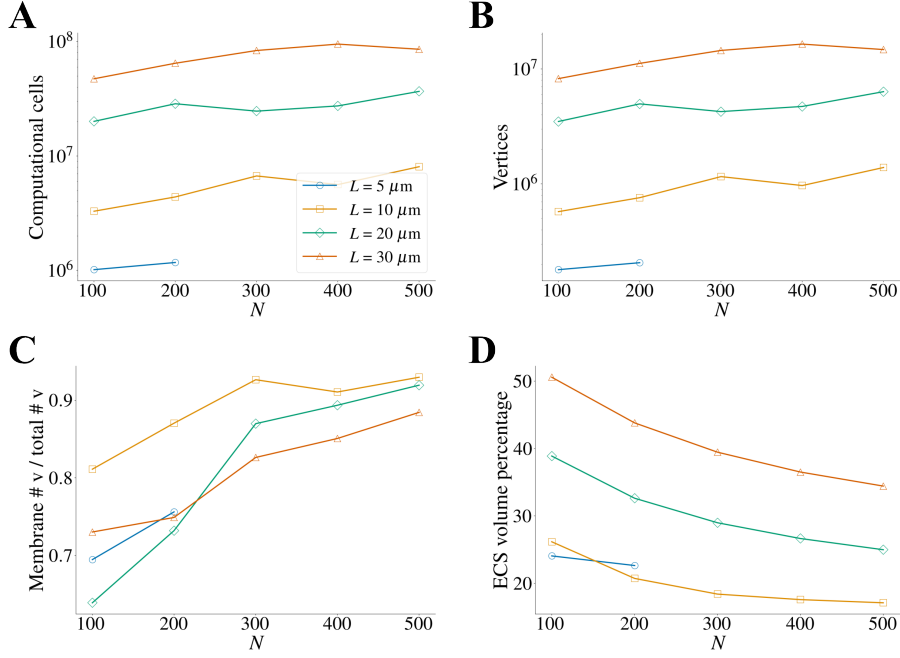


Fig. 4: Statistics of cellular geometries of mouse visual cortex tissue. (A) Total number of computational cells in the mesh. (B) Total number of mesh vertices. (C) The ratio of total number of membrane vertices to total number of mesh vertices. (D) Percentage of the total mesh volume that is occupied by extracellular space. Common legend for all subfigures.

is subdivided into intracellular space, extracellular space, and the cellular membranes that separate these spaces (Figure 5) [2]. We first state the general governing equations of electrodiffusion in cerebral tissue, before extending the equations to intracellular and extracellular spaces.

3.1 Governing equations of electrodiffusion

In the absence of fluid convection, the movement of ions in brain tissue is described by the Nernst-Planck equation, which states that the total flux $\mathbf{J}_k = \mathbf{J}_k(\mathbf{x}, t)$ of an ion k is a combination of molecular diffusion and electrical drift [61]:

$$\mathbf{J}_k = \mathbf{J}_{k,\text{diffusion}} + \mathbf{J}_{k,\text{drift}} = -D_k \nabla c_k - \frac{z_k D_k F}{RT} c_k \nabla \phi. \quad (1)$$

Here D_k and z_k are the free diffusion coefficient and valence of ion k , while $R = 8.314 \text{ Jmol}^{-1}\text{K}^{-1}$ is the universal gas constant, $T = 300 \text{ K}$ is absolute temperature and $F = 96485 \text{ Cmol}^{-1}$ is Faraday's constant. By assuming conservation of ions in the domain Ω , it follows that

$$\frac{\partial c_k}{\partial t} + \nabla \cdot \mathbf{J}_k = f_k \quad \text{in } \Omega, \quad (2)$$

where $f_k = f_k(\mathbf{x}, t)$ is a rate of addition or removal of ions.

An equation for the electric potential is derived by assuming bulk electroneutrality in the domain Ω . This is equivalent to no charge separation, meaning that the total sum of ion charges equals zero:

$$F \sum_{k=1}^K z_k c_k = 0. \quad (3)$$

One can derive an alternative form of (3) by differentiating the sum with respect to time, invoking (2), and assuming that the source terms f_k are electroneutral. This gives

$$F \sum_{k=1}^K z_k \nabla \cdot \mathbf{J}_k = 0. \quad (4)$$

In a discrete setting, the ellipticity of (4) can make this formulation favorable compared to (3). Coupling (3) or (4) with (1) and (2) has been studied in several works under several names [43, 23, 51, 18, 58]. Here we refer to this system of equations as the Kirchhoff-Nernst-Planck (KNP) equations.

3.2 Governing equations in multiple cells

Equations (1), (2) and (4) describe electroneutral electrodiffusion in the bulk of a domain Ω . We now turn to modeling excitable tissue where multiple cells communicate through the extracellular space across the cellular membranes. The model is based on the Extracellular-Membrane-Intracellular (EMI) framework, which considers separate domains for the extracellular space, the intracellular spaces, and the cellular membranes [65]. In principle, there can be N intracellular domains $\Omega_{i,j}$ for $j = 1, 2, \dots, N$ representing biological cells with a common extracellular domain Ω_e , with cellular membranes Γ_j denoting the interface between $\Omega_{i,j}$ and Ω_e . In this section, we describe the case with one biological cell ($N = 1$, Figure 5). The generalization to N non-intersecting biological cells is immediate.

Let $c_{k,r} = c_{k,r}(\mathbf{x}, t)$ be the ion concentrations and $\phi_r = \phi_r(\mathbf{x}, t)$ the electric potential in a domain Ω_r , where $r = \{i, e\}$ denotes the intra- or extracellular space. We continue to consider the ion set $K = \{\text{Na}^+, \text{K}^+, \text{Cl}^-\}$. Equations (1), (2) and (4) describe electrodiffusion in the bulk of the domains Ω_r :

$$\frac{\partial c_{k,r}}{\partial t} + \nabla \cdot \mathbf{J}_{k,r} = f_{k,r} \quad \text{in } \Omega_r, \quad (5)$$

$$F \sum_{k=1}^K z_k \nabla \cdot \mathbf{J}_{k,r} = 0 \quad \text{in } \Omega_r, \quad (6)$$

with the flux $\mathbf{J}_{k,r}$ given by the Nernst-Planck equation (1). As we have coupled the KNP equations with the EMI framework, we refer to (5) and (6) as the KNP-EMI equations.

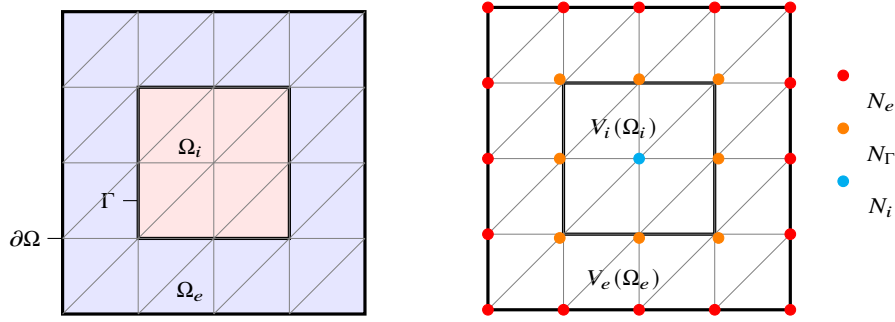


Fig. 5: Conceptual illustration of the geometry and meshes. Left: idealized geometry, illustrating the intracellular (Ω_i) and extracellular (Ω_e) spaces separated by a membrane Γ . The boundary of the domain is $\partial\Omega$. Right: The degree of freedom layout of the idealized cellular geometry when discretized with linear continuous Lagrange elements. The function spaces $V_i(\Omega_i)$ and $V_e(\Omega_e)$ share the degrees of freedom on Γ .

The intra- and extracellular dynamics are coupled at the cellular membrane Γ that separates the intra- and extracellular spaces. Cellular membranes in cerebral tissue are not freely permeable to ions, but lined with selective ion channels that only permit transport of select ions under specific circumstances. Because of this, there are spatial differences in the intra- and extracellular ion concentrations and thus a charge difference across the membrane. The concentration differences induce an electric potential difference across the membrane, labeled the membrane potential $\phi_m = \phi_i - \phi_e$, and the membrane acts like a capacitor storing electric energy [61]. On the cellular membrane Γ , we assume continuity in the membrane current density I_m :

$$I_m = F \sum_{k \in K} z_k \mathbf{J}_{k,i} \cdot \mathbf{n}_i = -F \sum_{k \in K} z_k \mathbf{J}_{k,e} \cdot \mathbf{n}_e, \quad \text{on } \Gamma \quad (7)$$

where the normal vector $\mathbf{n}_r = \mathbf{n}_r(\mathbf{x})$ is directed out of the domain Ω_r .

We will here consider the *single-dimensional* form of the KNP-EMI equations, where the membrane current density I_m that exists on a lower-dimensional manifold is eliminated from the system of equations [65, 5, 18]. We assume that the membrane current I_m is the sum of an ionic current I_{ion} , whose model depends on the physiological

scenario considered, and a capacitive current I_{cap} , which reflects the electric energy stored in the membrane. Assuming that the membrane is a parallel plate capacitor with capacitance C_m , the capacitive current is

$$I_{\text{cap}} = C_m \frac{\partial \phi_m}{\partial t}. \quad (8)$$

We assume that both the ionic current and the capacitive current has ion-specific contributions:

$$I_{\text{ion}} + I_{\text{cap}} = \sum_{k \in K} I_{\text{ion},k} + \sum_{k \in K} I_{\text{cap},k}, \quad (9)$$

with

$$I_{\text{cap},k} = \alpha_{k,r} I_{\text{cap}} \quad (10)$$

weighted by the coefficients

$$\alpha_{k,r} = \frac{z_k^2 D_{k,r} c_{k,r}}{\sum_{l \in K} z_l^2 D_{l,r} c_{l,r}}. \quad (11)$$

By definition $\sum_{k \in K} \alpha_{k,r} = 1$. Using (11) and (10) with the relation (9) and the definition of the membrane current (7), the flux of an ion k is expressed as a function of the ionic currents and the membrane potential

$$\mathbf{J}_{k,r} \cdot \mathbf{n}_r = \pm_r \frac{I_{\text{ion},k} + I_{\text{cap},k}}{F z_k} = \pm_r \frac{I_{\text{ion},k} + \alpha_{k,r} C_m \frac{\partial \phi_m}{\partial t}}{F z_k} \quad (12)$$

for $r \in \{i, e\}$, with the signs $\pm_i = 1$ and $\pm_e = -1$.

3.3 Membrane mechanisms and stimulus

Cellular membrane mechanisms such as ion channels, pumps and cotransporters are central to excitable tissue dynamics. The membrane mechanisms determine how cells respond to external stimuli such as synaptic signaling, or to changes in the extracellular environment. When modelling membrane mechanisms, one considers the cell types and biological scenarios at hand. For example, neurons and astrocytes have different membrane mechanisms [2, 25]. Here, we let neuronal membrane dynamics be governed by the Hodgkin-Huxley model [28], an Na^+/K^+ -ATPase pump [33] and the two cotransporters KCC2 and NKCC1 [69, 17]. Glial membrane dynamics are governed by an ATP pump [25], passive leak channels with an inward-rectifying potassium current [25], and the KCC1 and NKCC1 cotransporters [45].

The Hodgkin-Huxley model [28] enables simulating action potentials, the communicating signal of neurons. The model includes ion channel currents that are voltage-gated; i.e., whether they are open or closed depend on the difference between a resting membrane potential ϕ_{rest} and an ion-specific reversal potential E_k . The Hodgkin-Huxley model includes passive (leak) channels and active channels. Letting $g_{k,\text{leak}}$ be the con-

ductance of the leak channel of ion k , the general expression for a neuronal leak channel current is

$$I_{\text{leak},k,n} = g_{\text{leak},k,n}(\phi_m - E_k).$$

The reversal potential

$$E_k = \frac{RT}{z_k F} \log \frac{c_{k,e}}{c_{k,i}},$$

follows from the Nernst-Planck equation, considering a steady state where the diffusive flux balances the electrical drift across the cellular membrane [61].

The active channels include gating variables n, m and h that reflect the probability that an ion channel is open or closed. For sodium and potassium, the active channel currents are

$$\begin{aligned} I_{\text{active,Na}} &= \bar{g}_{\text{Na}} m^3 h (\phi_m - E_{\text{Na}}), \\ I_{\text{active,K}} &= \bar{g}_{\text{K}} n^4 (\phi_m - E_{\text{K}}), \end{aligned}$$

where \bar{g}_k is the maximum conductivity of the channel for ion k . There is no active channel for chloride. Time evolution of the gating variables n, m, h is governed by ordinary differential equations (ODEs) of the general form

$$\frac{\partial \zeta}{\partial t} = \alpha_\zeta (1 - \zeta) - \beta_\zeta \zeta, \quad (13)$$

where $\zeta = (n(t), m(t), h(t))$. The coefficients α_ζ and β_ζ depend on the difference $\phi_m - \phi_{\text{resting}}$. The ODEs (13) are equipped with appropriate initial conditions $\zeta(t = 0) = \zeta_0 = (n_0, m_0, h_0)$. See [28] for full comprehensive details of the model and its coefficients.

In addition to passive and active ion channels, which are driven by the difference $\phi_m - E_k$, we model membrane mechanisms that are driven by differences in intra- and extracellular concentrations. First, we consider the sodium-potassium pump Na^+/K^+ -ATPase. This pump uses ATP (adenosine triphosphate) as energy to pump sodium out of a cell and potassium into the cell. For every ATP molecule consumed, three sodium ions are exported and two potassium ions are imported, meaning the pump is a net exporter of electric charge. The membrane current density associated with the ATP pump on neuronal cell membranes is modeled by

$$I_{\text{ATP},n} = \frac{S_{\text{ATP},n}}{(1 + P_{\text{K}}/c_{\text{K},e})^2 (1 + P_{\text{Na}}/c_{\text{Na},i})^3},$$

where $S_{\text{ATP},n} = 0.25 \text{ Am}^{-2}$ is the pump strength, while $P_{\text{K}} = 1.5 \text{ mM}$ and $P_{\text{Na}} = 10 \text{ mM}$ are threshold values that determine when the pump strength increases and decreases [47, 33].

For the neuronal membranes, we also consider the two cotransporters NKCC1 and KCC2. The NKCC1 cotransporter transports sodium, potassium and chloride into the cell, while the KCC2 cotransporter transports potassium and chloride out of cells [69, 17, 47]. The membrane current densities associated with the cotransporters are defined as

$$I_{\text{NKCC1},n} = \delta S_{\text{NKCC1},n} \ln \frac{c_{\text{K},e} c_{\text{Cl},e}}{c_{\text{K},i} c_{\text{Cl},i}},$$

$$I_{\text{KCC2}} = S_{\text{KCC2}} \ln \frac{c_{\text{Na},e} c_{\text{K},e} c_{\text{Cl},e}^2}{c_{\text{Na},i} c_{\text{K},i} c_{\text{Cl},i}^2},$$

where $S_{\text{NKCC1},n} = 0.0023 \text{ Am}^{-2}$ and $S_{\text{KCC2}} = 0.0068 \text{ Am}^{-2}$ are the maximum strengths of the cotransporters. The function $\delta = \delta(c_{\text{K},e}^0, c_{\text{K},e})$ is defined as

$$\delta(c_{\text{K},e}^0, c_{\text{K},e}) = \frac{1.0}{(1.0 + (0.03/(c_{\text{K},e} - c_{\text{K},e}^0))^{10})} \quad (14)$$

if $c_{\text{K},e} \in [3.0, c_{\text{K},e}^0]$, else $\delta = 0$ to suppress activity of the NKCC1 cotransporter [47].

For glial cells, we consider mechanisms described in previous astrocyte modeling studies [45, 25, 47]. We define the glial leak channel currents with different conductances than for the neuronal cells

$$I_{\text{leak},k,g} = g_{\text{leak},k,g} f_{\text{Kir-Na},k}(\phi_m - E_k),$$

where

$$f_{\text{Kir-Na},k} = \begin{cases} 1.0, & \text{for } k \in \{\text{Na}, \text{Cl}\}, \\ \sqrt{\frac{c_{\text{K},e}}{c_{\text{K},e}^0}} \frac{AB}{CD}, & \text{for } k = \text{K}. \end{cases} \quad (15)$$

This function is used to model the potassium leak channel as inward-rectifying [25]. In Equation (15), $c_{\text{K},e}^0$ is the initial extracellular potassium concentration, while the coefficients A, B, C and D are defined as

$$A = 1 + e^{0.433},$$

$$B = 1 + e^{\frac{-(0.1186 + E_{\text{K}}^0)}{0.0441}},$$

$$C = 1 + e^{\frac{(\phi_m - E_{\text{K}} + 0.0185)}{0.0425}},$$

$$D = 1 + e^{\frac{-(0.1186 + \phi_m)}{0.0441}},$$

where E_{K}^0 is the initial potassium Nernst potential.

We model a Na^+/K^+ -ATPase pump current and cotransporters for glia, similar to the approach for neurons. The glial ATP pump current density is expressed as

$$I_{\text{ATP},g} = \frac{S_{\text{ATP},g}}{(1 + P_{\text{K}}/c_{\text{K},e})(1 + P_{\text{Na}}/c_{\text{Na},i})^{3/2}},$$

where $S_{\text{ATP},g} = 0.12 \text{ Am}^{-2}$, $P_{\text{Na}} = 10 \text{ mM}$ and $P_{\text{K}} = 1.5 \text{ mM}$ are the maximum pump strength, sodium and potassium pump thresholds, respectively [45, 25].

For glia, we consider the NKCC1 and KCC1 cotransporters [45, 47]. The membrane current densities associated with these cotransporters are

$$I_{\text{NKCC1},g} = \delta S_{\text{NKCC1},g} \ln \frac{c_{\text{K},e} c_{\text{Cl},e}}{c_{\text{K},i} c_{\text{Cl},i}},$$

$$I_{\text{KCC1}} = S_{\text{KCC1}} \ln \frac{c_{\text{Na},e} c_{\text{K},e} c_{\text{Cl},e}^2}{c_{\text{Na},i} c_{\text{K},i} c_{\text{Cl},i}^2},$$

where the maximum cotransporter strengths are $S_{\text{NKCC1},g} = 5.2 \times 10^{-4} \text{ Am}^{-2}$ and $S_{\text{KCC1}} = 0.018 \text{ Am}^{-2}$, and δ is given by Equation (14).

We stimulate the brain tissue through adding a stimulus current density to the sodium ionic current density. We model an exponentially decreasing stimulus with the expression

$$I_{\text{stim}} = \bar{g}_{\text{stim}} e^{(-t \bmod T_{\text{stim}})/a_{\text{stim}}}. \quad (16)$$

Here \bar{g}_{stim} is the maximum stimulus conductance. The exponential factor in Equation (16) makes I_{stim} decay exponentially with a time constant $a_{\text{stim}} = 0.5 \text{ ms}$, and the modulus operation is to turn the current on periodically with a period T_{stim} .

To summarize, the ionic current densities for neuronal cell membranes are

$$I_{\text{ion,Na},n} = I_{\text{leak,Na},n} + I_{\text{active,Na}} + I_{\text{stim}} + 3I_{\text{ATP},n} - I_{\text{NKCC1},n},$$

$$I_{\text{ion,K},n} = I_{\text{leak,K}} + I_{\text{active,K}} - 2I_{\text{ATP},n} - I_{\text{NKCC1},n} - I_{\text{KCC2}},$$

$$I_{\text{ion,Cl},n} = I_{\text{leak,Cl}} + 2I_{\text{NKCC1},n} + I_{\text{KCC2}},$$

while in the cases where we consider glial cells, the glial ionic membrane current densities are

$$I_{\text{ion,Na},g} = I_{\text{leak,Na},g} + I_{\text{active,Na}} + 3I_{\text{ATP},g} - I_{\text{NKCC1},g},$$

$$I_{\text{ion,K},g} = I_{\text{leak,K}} - 2I_{\text{ATP},g} - I_{\text{NKCC1},g} - I_{\text{KCC1}},$$

$$I_{\text{ion,Cl},g} = I_{\text{leak,Cl},g} + 2I_{\text{NKCC1},g} + I_{\text{KCC1}}.$$

3.4 Boundary conditions

With the membrane currents defined, it remains to determine boundary and initial conditions to close the KNP-EMI equation system. As boundary conditions, we consider a no-flux condition on all boundaries $\partial\Omega_r$ exterior to the domain Ω_r for all times $t > 0$:

$$\mathbf{J}_{k,r} \cdot \mathbf{n}_r = 0, \quad \forall k \quad \text{on } \partial\Omega_r, \quad \forall r. \quad (17)$$

With the boundary condition (17) enforced on all boundaries, the electric potentials are only determined up to a constant. We return to this point in Section 4.3.

3.5 Initial conditions and defining resting states

As initial conditions, we set the initial concentrations $c_{k,r}(\mathbf{x}, 0) = c_{k,r}^0$ and electric potentials $\phi_r(\mathbf{x}, 0) = \phi_r^0$.

To define initial conditions that constitute a resting state with no changes in ionic concentrations or electrical potentials, we solve a system of ordinary differential equations (ODEs) that represent the dynamics in a single spatial point. When only considering neurons, we collapse the intracellular spaces and the extracellular space into two separate compartments. When modeling both neuronal and glial cells, we consider two separate intracellular compartments, one for each cell type, and a third compartment for the extracellular space. In these compartmental models, the change in the membrane potential at steady state is given by the total ionic current I_{ion} , since then the total membrane current density $I_m = I_{\text{ion}} + I_{\text{cap}} = 0$. The ion concentration changes are in turn given by the molar fluxes associated with the total ionic current densities of the respective ions. The resulting steady-state ODE system for the three-compartment model is

$$\begin{aligned} \frac{d\phi_{m,l}}{dt} &= -\frac{1}{C_m} I_{\text{ion},l}, \\ \frac{dc_{k,i,l}}{dt} &= -\frac{I_{\text{ion},k,l}}{z_k F} \frac{|\Gamma|_l}{|\Omega|_{i,l}}, \\ \frac{dc_{k,e}}{dt} &= \frac{1}{z_k F} \left(I_{\text{ion},k,n} \frac{|\Gamma|_n}{|\Omega|_e} + I_{\text{ion},k,g} \frac{|\Gamma|_g}{|\Omega|_e} \right), \\ \frac{d\zeta}{dt} &= \alpha_\zeta (1 - \zeta) - \beta_\zeta \zeta. \end{aligned} \tag{18}$$

This ODE system respects our convention of considering currents out of a cell as negative fluxes. The subscript $l \in \{n, g\}$ denotes neuronal or glial cell, $|\Gamma|_l$ is the total surface area of the cellular membranes separating the compartment of cell type l from the extracellular space, $|\Omega|_{i,l}$ is the total volume of all intracellular compartments of cell type l , and $|\Omega|_e$ is the volume of the extracellular space. The two-compartment system results from reducing (18) by considering only $l = n$. A steady-state solution to the system (18) will constitute a steady state for the full PDE system, given that we set the initial condition constant in space and that the membrane mechanisms are homogeneous in space.

To determine initial conditions for the PDE system by solving the ODE system (18), we consider a set of initial conditions for the ODE system. The initial membrane potentials used to solve the ODE system are -70 mV and -85 mV for the neurons and astrocytes, respectively (taken from [5, 47, 46]). The initial concentrations are based on physiological concentrations in neurons and glial cells (taken from [13, 46, 47, 45]). Finally, the initial conditions for the gating variables are set by solving (13) at steady state with $\phi_m = -70$ mV. All the membrane mechanism parameters and physical constants in the KNP-EMI model used in this work are listed in Table 2. We note that some of the membrane mechanism parameters were calibrated to achieve balance between the membrane mechanisms.

Table 2: Material and model parameters. (*) Used to determine initial conditions with a steady-state approximation. (†) Calibrated based on reference.

Parameter	Symbol	Value	Unit	Ref.
Universal gas constant	R	8.314	$\text{JK}^{-1}\text{mol}^{-1}$	
Faraday constant	F	96485	Cmol^{-1}	
Temperature	T	300	K	
Free diffusion coefficient sodium	D_{r,Na^+}	1.33×10^{-9}	m^2s^{-1}	[27]
Free diffusion coefficient potassium	D_{r,K^+}	1.96×10^{-9}	m^2s^{-1}	[27]
Free diffusion coefficient chloride	D_{r,Cl^-}	2.03×10^{-9}	m^2s^{-1}	[27]
Initial neuronal sodium concentration (ICS)	$[\text{Na}^+]_{i,n}^0$	10	mM	[13]*
Initial glial sodium concentration (ICS)	$[\text{Na}^+]_{i,g}^0$	15	mM	[47]*
Initial sodium concentration (ECS)	$[\text{Na}^+]_e^0$	145	mM	[47]*
Initial neuronal potassium concentration (ICS)	$[\text{K}^+]_{i,n}^0$	130	mM	[13]*
Initial glial potassium concentration (ICS)	$[\text{K}^+]_{i,g}^0$	100	mM	[47]*
Initial potassium concentration (ECS)	$[\text{K}^+]_e^0$	3	mM	[47]*
Initial neuronal chloride concentration (ICS)	$[\text{Cl}^-]_{i,n}^0$	5	mM	[13]*
Initial glial chloride concentration (ICS)	$[\text{Cl}^-]_{i,g}^0$	5	mM	[47]*
Initial chloride concentration (ECS)	$[\text{Cl}^-]_e^0$	134	mM	[47]*
Initial neuronal membrane potential	$\phi_{m,n}^0$	-70	mV	[61]*
Initial glial membrane potential	$\phi_{m,g}^0$	-85	mV	[47]*
Resting membrane potential	ϕ_{resting}	-65	mV	
Membrane capacitance	C_m	0.01	Fm^{-2}	[47]
Initial potassium activation probability	n_0	0.244		*
Initial sodium activation probability	m_0	0.029		*
Initial sodium inactivation probability	h_0	0.754		*
Sodium maximum conductivity	\bar{g}_{Na}	1200	Sm^{-2}	[28]
Potassium maximum conductivity	\bar{g}_{K}	360	Sm^{-2}	[28]
Neuronal sodium leak conductivity	$g_{\text{Na,leak},n}$	0.3	Sm^{-2}	[5]†
Glial sodium leak conductivity	$g_{\text{Na,leak},g}$	1	Sm^{-2}	[45]
Neuronal potassium leak conductivity	$g_{\text{K,leak},n}$	0.1	Sm^{-2}	[47]†
Glial potassium leak conductivity	$g_{\text{K,leak},g}$	16.96	Sm^{-2}	[45]
Neuronal chloride leak conductivity	$g_{\text{Cl,leak},n}$	0.25	Sm^{-2}	[45]
Glial chloride leak conductivity	$g_{\text{Cl,leak},g}$	2.0	Sm^{-2}	[45]†
Neuronal ATP pump maximum strength	$S_{\text{ATP},n}$	0.25	Am^{-2}	[33, 16]†
Glial ATP pump maximum strength	$S_{\text{ATP},g}$	0.12	Am^{-2}	[25]†
ATP pump sodium threshold	P_{Na}	10	mM	[25]
ATP pump potassium threshold	P_{K}	1.5	mM	[25]
Neuronal NKCC1 maximum strength	$S_{\text{NKCC1},n}$	0.0023	Am^{-2}	[17]†
Glial NKCC1 maximum strength	$S_{\text{NKCC1},g}$	5.2×10^{-4}	Am^{-2}	[45]
KCC2 maximum strength	S_{KCC2}	0.0068	Am^{-2}	[17]†
KCC1 maximum strength	S_{KCC1}	0.018	Am^{-2}	[45]
Stimulus time constant	a_{stim}	5×10^{-4}	s	
Maximum stimulus conductance	\bar{g}_{stim}	60–500	Sm^{-2}	

4 Discretization and numerical solution of the KNP-EMI equations

The KNP-EMI model equations can be summarized as follows: find the ionic concentrations $c_{k,r} = c_{k,r}(\mathbf{x}, t)$ and electric potentials $\phi_r = \phi_r(\mathbf{x}, t)$ in the domains Ω_r such

that for all $t \in [0, T]$

$$\frac{\partial c_{k,r}}{\partial t} + \nabla \cdot \mathbf{J}_{k,r} = f_{k,r} \quad \text{in } \Omega_r, \quad (19a)$$

$$F \sum_{k=1}^K z_k \nabla \cdot \mathbf{J}_{k,r} = 0 \quad \text{in } \Omega_r, \quad (19b)$$

$$\mathbf{J}_{k,r} \cdot \mathbf{n}_r = \pm_r \frac{I_{\text{ion},k} + \alpha_{k,r} C_m \frac{\partial \phi_m}{\partial t}}{F z_k} \quad \text{on } \Gamma, \quad (19c)$$

$$\mathbf{J}_{k,r} = -D_{k,r} \nabla c_{k,r} - \frac{z_{k,r} D_{k,r} F}{RT} c_{k,r} \nabla \phi_r \quad \text{in } \Omega_r, \quad (19d)$$

$$c_{k,r}(\mathbf{x}, 0) = c_{k,r}^0 \quad \text{in } \Omega_r, \quad (19e)$$

$$\phi_r(\mathbf{x}, 0) = \phi_r^0 \quad \text{in } \Omega_r, \quad (19f)$$

$$\mathbf{J}_{k,r} \cdot \mathbf{n}_r = 0 \quad \text{on } \partial\Omega_r. \quad (19g)$$

We solve these equations using the solution algorithm presented by Benedusi *et al.* [5]. The scheme is based on a finite difference method in time, an operator splitting scheme decoupling the ODEs from the PDEs, a finite element spatial discretization, and finally an iterative, preconditioned solver for the resulting linear system. For completeness, we describe the solution steps in detail below.

4.1 Operator splitting and time discretization

The KNP-EMI equations are nonlinear, involving both a bilinear coupling of each concentration field with the electric potential in each bulk domains Ω_r cf. (19d) and nonlinear dynamics at the membrane cf. (19c). The bulk and membrane dynamics occur on different timescales, with much faster membrane dynamics. To decouple across these different scales, we consider an implicit-explicit operator splitting scheme [18, 5]. To this end, we first partition the time interval $[0, T]$ uniformly into times¹ $t^n = n\Delta t$ with $n = 1, \dots, N_t$ for N_t timesteps with timestep size Δt . At each timestep t^n , given the membrane potential at the previous timestep, we first solve the gating variable ODEs (13) to obtain an approximation of the ionic currents $I_{\text{ion},k}$. Specifically, we solve the ODEs from t^{n-1} to t^n using m steps of a Rush-Larsen method [52] with a local timestep $\Delta t_{\text{ODE}} = \Delta t/m$ (we let $m = 25$). Next, we discretize (19a) and (19c) in time using an implicit Euler method, and solve (19a)–(19d) by evaluating the just-computed ionic currents directly. We linearize the bilinear term by evaluating the concentration in the electrical drift term and in the coefficients $\alpha_{k,r}$ at the previous timestep.

¹ Since the unknown variables already have an ion index k and a domain index r , we denote the timestep n by a superscript to avoid a triple subscript.

4.2 Finite element spatial discretization

Our computational meshes are composed of tessellated intracellular domains \mathcal{T}_i and extracellular space \mathcal{T}_e (Figure 5). In this section, we present the finite element discretization for just one connected intracellular domain. This extends to N disjoint intracellular domains readily, as will be demonstrated in Section 5. Relative to each mesh domain \mathcal{T}_r , we define the finite element space of continuous piecewise linear polynomials $V(\mathcal{T})$. The fully discrete weak form of the "PDE part" of the KNP-EMI problem then reads: at each time t^n , find the concentration $c_{k,r}^{n,h} \in V(\mathcal{T}_r)$ for $k \in K$ and electric potentials $\phi_r^{n,h} \in V(\mathcal{T}_r)$ such that

$$\begin{aligned} \int_{\Omega_r} \left(c_{k,r}^{n,h} v_{k,r} - \Delta t \mathbf{J}_{k,r}^{n,h} \cdot \nabla v_{k,r} \right) dx \pm_r \frac{\alpha_{k,r}^n C_m}{z_k F} \int_{\Gamma} \phi_m^{n,h} v_{k,r} ds \\ = \int_{\Omega_r} \left((c_{k,r}^{n-1,h} + \Delta t f_{k,r}^n) v_{k,r} \right) dx - \int_{\Gamma} g_{k,r}^{n-1,h} v_{k,r} ds \end{aligned} \quad (20)$$

for all $v_{k,r} \in V(\mathcal{T}_r)$, $k \in K$, $r \in \{i, e\}$, and

$$- \Delta t \sum_{k \in K} z_k \int_{\Omega_r} \mathbf{J}_{k,r}^{n,h} \cdot \nabla w_r dx \pm_r \frac{C_m}{F} \int_{\Gamma} \phi_m^{n,h} w_r ds = - \int_{\Gamma} q_r^{n-1,h} w_r ds \quad (21)$$

for all $w_r \in V(\mathcal{T}_r)$. Here, we have introduced the short-hand

$$g_{k,r}^{n,h} = \pm_r \frac{1}{z_k F} \left(\Delta t I_{\text{ion},k}^{n,h} - \alpha_{k,r}^n C_m \phi_m^{n,h} \right) \text{ and } q_r^{n,h} = \pm_r \left(\Delta t I_{\text{ion},k}^{n,h} - C_m \phi_m^{n,h} \right) / F. \quad (22)$$

The discrete weak form induces a linear system $\mathbf{A}^n \mathbf{x}^n = \mathbf{b}^n$ to be solved at every timestep n . The system matrix \mathbf{A}^n has the following block structure:

$$\mathbf{A}^n = \begin{bmatrix} \mathbf{A}_{c,i} & \mathbf{B}_i & 0 & 0 \\ \mathbf{B}_i^T & \mathbf{A}_{\phi,i} & \mathbf{C}_{i,e} & \mathbf{D}_{i,e} \\ 0 & \mathbf{C}_{e,i} & \mathbf{A}_{c,e} & \mathbf{B}_e \\ 0 & \mathbf{D}_{e,i} & \mathbf{B}_e^T & \mathbf{A}_{\phi,e} \end{bmatrix}^n \quad (23)$$

where $\mathbf{A}_{f,r}$ is the stiffness matrix for function f in the domain r , \mathbf{B}_r is the membrane potential coupling stiffness matrix, \mathbf{C}_{r_1,r_2} is the concentration-potential coupling block between space r_1 and r_2 , and \mathbf{D}_{r_1,r_2} are the potential coupling blocks. Note that $\mathbf{A}_{c,r}$ are block matrices with each of the individual $\mathbf{A}_{c_k,i}$ stiffness matrices on the diagonal. The blocks in (23) coupling the intra- and extracellular spaces arise from the shared degrees of freedom on the cellular membranes (Figure 5).

4.3 Solving the KNP-EMI equations in dense cortical tissue geometries

We solve the linear KNP-EMI PDE system (23) in a monolithic fashion using an iterative method as previously described [5]. The iterative solver uses a Generalized Minimal Residual Method (GMRES) [53] and is preconditioned with an Algebraic Multigrid (AMG) method [70, 30]. We use

$$P = \begin{bmatrix} A_{c,i} & 0 & 0 & 0 \\ 0 & A_{\phi,i} & 0 & 0 \\ 0 & 0 & A_{c,e} & 0 \\ 0 & 0 & 0 & A_{\phi,e} \end{bmatrix}$$

as a preconditioner for the linear system, where all of the stiffness matrices are evaluated with the initial conditions. We noted previously that our choice of boundary conditions leaves the electric potentials only determined up to a constant. Thus, without additional constraints, the matrix A^n (23) is singular. We address this by providing the iterative solver with the nullspace of A^n , which is the set of all constants. We also orthogonalize b^n with respect to the nullspace.

The computational model is implemented in DOLFINx [4], which is interfaced with the linear algebra library PETSc. The software is parallelized with MPI communication. The model implementation was verified in two ways (Section 6): (i) a convergence study on idealized geometries; (ii) a convergence study on the mouse visual cortex meshes. The implementation is openly available at Github: <https://github.com/hherlyng/knp-emi-cgx>.

The key question now is how this numerical solution strategy performs in realistic or near realistic simulation scenarios defined over dense cortical tissue geometries. To study this, we simulate the firing of an action potential within the cortical tissue geometries generated in Section 2. In each geometry, the axon of one of the neurons is stimulated by a stimulus current density as introduced in Section 3.3. As an example of the setup, Figure 6A shows the geometry for the mesh with $L = 5 \mu\text{m}$ and $N = 100$, with the stimulated axon in pink. For simplicity in this performance test case, we consider all other intracellular domains within the tissue cube to also be neurons, by employing the neuronal membrane mechanisms (as introduced in Section 3.3).

The simulations are run for a total of 200 timesteps with $\Delta t = 2.5 \times 10^{-5}$ s to a final time of 5 ms. The total stimulus current applied on the neuronal membrane (Figure 6B) makes the membrane potential cross the threshold required for firing a single action potential (Figure 6C). We note that the simulations are run with a varying amount of processes for varying L to achieve reasonable runtimes as the problem sizes increase (Table 3). All simulations were run using the high-performance computing architecture eX3 [37] on a node with two AMD EPYC Genoa-X 9684X 96-Core dualprocessors.

We first examine the total assembly times – the total time spent assembling the system matrix, right-hand side vector and preconditioner matrix over the whole simulation time (Table 4). As expected, these times increase with increasing problem size in a controlled fashion. A general trend is that assembly times remain fairly constant when concomitantly doubling the number of MPI cores and the number of degrees of freedom, indicating scalable assembly.

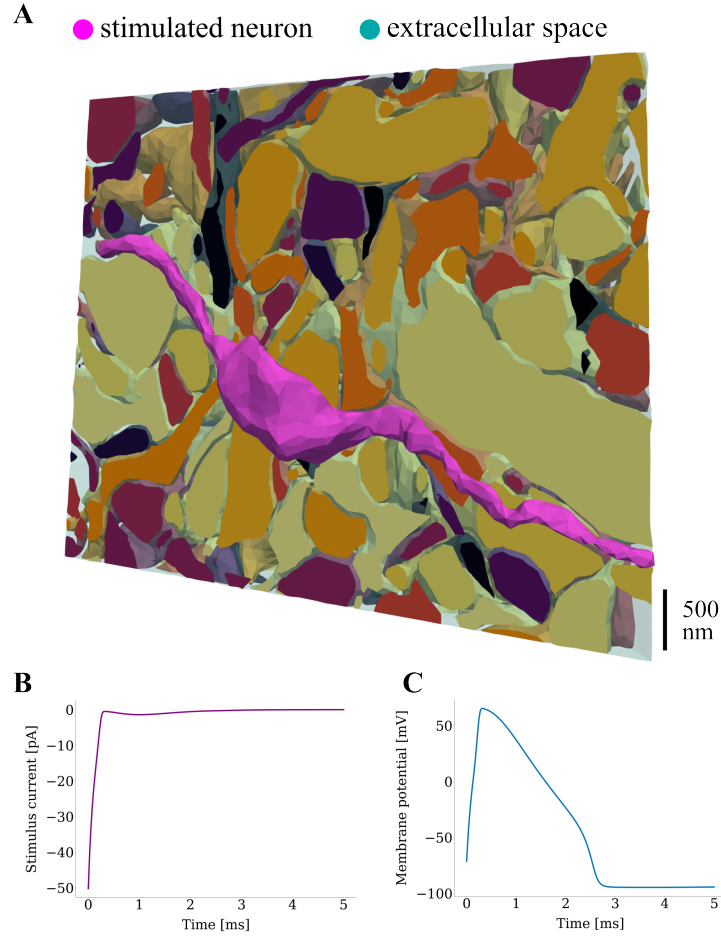


Fig. 6: Simulation setup to test the performance of the iterative linear solver. **A.** A clip of the $L = 5 \mu\text{m}$, $N = 100$ geometry with a central axon highlighted in pink. The extracellular space is shown in light blue, while the remaining cells or cell fragments are shown in separate, unique colors. **B.** The total stimulus current applied to the membrane of the axon through adding a sodium stimulus current to the ionic membrane current density. **C.** The membrane potential measured in a point on the axon's membrane ($\mathbf{x} = (1186, 3241, 3594) \text{ nm}$).

Table 3: Problem sizes (numbers of degrees of freedom) on the mouse visual cortex meshes with varying domain boundary side lengths L and total number of biological cells N . The – entries signify that there are no meshes for $L = 5 \mu\text{m}$ and $N > 200$.

$L [\mu\text{m}]$	$N = 100$	$N = 200$	$N = 300$	$N = 400$	$N = 500$
5	1 219 172	1 452 136	–	–	–
10	4 161 248	5 683 448	8 926 676	7 401 376	10 729 424
20	22 892 896	34 403 796	31 837 296	35 739 444	48 709 344
30	57 002 756	78 171 324	105 776 564	121 689 728	111 075 140

Table 4: Assembly times when simulating an action potential on the mouse visual cortex meshes with varying domain boundary side lengths L and total number of biological cells N . The – entries signify that there are no meshes for $L = 5 \mu\text{m}$ and $N > 200$.

$L [\mu\text{m}]$	$N = 100$	$N = 200$	$N = 300$	$N = 400$	$N = 500$
5 (16 cores)	1390 s	1783 s	–	–	–
10 (32 cores)	2269 s	3459 s	5543 s	5414 s	8314 s
20 (64 cores)	7219 s	10749 s	10260 s	12751 s	16355 s
30 (128 cores)	7597 s	14828 s	21652 s		

Turning to look at per-timestep linear solver iterations until convergence, the number of iterations is highest during the action potential when the variables rapidly change with time (Figure 7). After the membrane potential peak around timestep 25, iteration counts remain fairly constant until a slight increase concurrent with the membrane potential kink at around timestep 100. For the last 100 iterations the iteration counts fall at first before stabilizing, as a result of the membrane potential being fairly constant.

The solver performance in terms of average iterations is stable for the smaller geometries with $L = 5 \mu\text{m}$ and $L = 10 \mu\text{m}$, and for the $L = 20 \mu\text{m}$ geometries with up to $N = 300$ biological cells, while the iteration counts start increasing from $N = 300$ towards $N = 500$ (Table 5). For the $L = 30 \mu\text{m}$ geometries, iteration counts are higher than the smaller geometries and increase with increasing N . For $N = 400$ and $N = 500$, the linear solver reached the prescribed maximum number of iterations per timestep (5000). The total time spent solving the linear system generally increases as problem sizes increase.

We now look at strong scaling of the solver by comparing performance on the $L = 10 \mu\text{m}$ geometries when using 16 and 32 cores. Assembly times are roughly cut in half when doubling the number of cores (Table 6). The solver times are halved for the $N = 100$ and $N = 400$ geometries, and even more than halved for the $N = 200$ geometry. Mostly, the average number of iterations are similar when running on 16 and 32 cores. An interesting exception is the $N = 300$ geometry, for which the average iteration count almost doubles when doubling the number of cores.

In summary, these findings indicate that the solution strategy performs well for reasonably complex meshes, but also that there are clear opportunities for further research in solution algorithms for simulation of electrodifusion in dense tissue reconstructions.

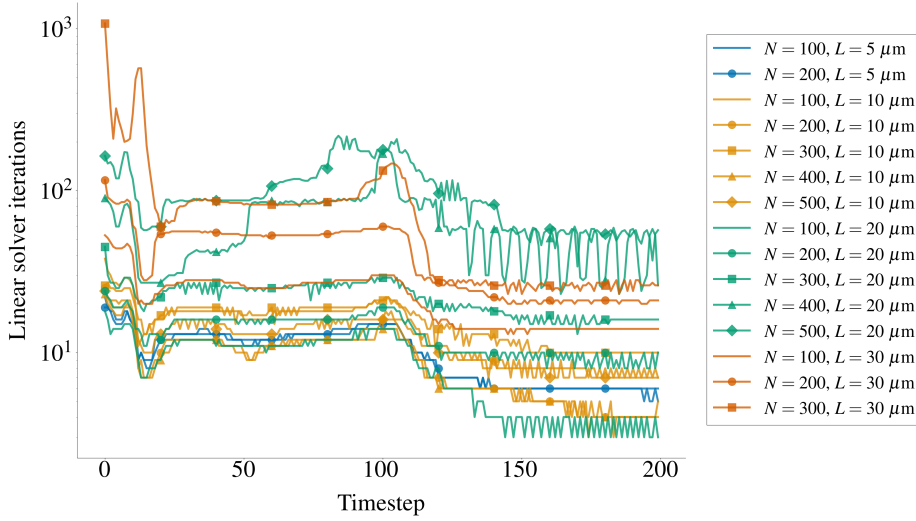


Fig. 7: Iteration counts for 200 timesteps when solving the KNP-EMI equations on the various mouse visual cortex geometries during a simulation of an action potential. Note the logarithmic scaling of the vertical axis.

Table 5: Solver times (in seconds) and average iteration counts (in brackets) when simulating an action potential on the mouse visual cortex meshes with varying domain boundary side lengths L and total number of biological cells N . The – entries signify that there are no meshes for $L = 5 \mu\text{m}$ and $N > 200$. Max its. means the simulation exceeded the prescribed maximum number of linear solver iterations for a single timestep (5000).

$L [\mu\text{m}]$	$N = 100$	$N = 200$	$N = 300$	$N = 400$	$N = 500$
5 (16 cores)	175 s [10]	203 s [10]	–	–	–
10 (32 cores)	435 s [14]	443 s [9]	1103 s [16]	648 s [9]	1263 s [12]
20 (64 cores)	1105 s [9]	2316 s [13]	3258 s [22]	10400 s [62]	21172 s [100]
30 (128 cores)	3206 s [22]	10901 s [40]	30127 s [86]	max its.	max its.

Table 6: Solver times and average iteration counts when simulating an action potential on the mouse visual cortex meshes with the $L = 10 \mu\text{m}$ geometries for varying number of biological cells N .

Metric (# Cores)	$N = 100$	$N = 200$	$N = 300$	$N = 400$	$N = 500$
Assembly (16)	4796 s	7621 s	12354 s	10745 s	15819 s
Assembly (32)	2269 s	3459 s	5543 s	5414 s	8314 s
Solve (16)	844 s	1283 s	1443 s	1204 s	2578 s
Solve (32)	435 s	443 s	1103 s	648 s	1263 s
Average iterations (16)	13	13	9	9	15
Average iterations (32)	14	9	16	9	12

5 Electrodiffusive interplay in geometrically detailed brain tissue during low- and high-frequency firing

Neuronal activity is governed by ionic movement across cellular membranes. A key change is the release of potassium from excited neurons into the extracellular space (ECS), which, if not cleared efficiently, can enhance neuronal excitability and disrupt neuronal function [3, 44, 67]. The restoration of extracellular ionic levels, via e.g. glial uptake or homeostatic mechanisms such as the Na^+/K^+ -ATPase sodium-potassium pump, following neuronal activity is thus critical for healthy brain function [36, 68]. During sustained high-frequency firing, the homeostatic mechanisms are not able to keep up, leading to larger, persistent ionic shifts that will alter excitability and firing patterns [59]. The intricate morphology of individual cells and the surrounding ECS may further affect local electrodiffusive dynamics, a factor often neglected in simplified models.

To demonstrate the capabilities of the electrodiffusive simulation framework detailed in the present work, we consider the two scenarios (i) low-frequency (normal) neuronal activity and (ii) high-frequency firing, in a geometrically detailed domain with neurons, glial cells and ECS. We analyze and compare the two scenarios and point to observations where shape affects the dynamics (and thus potentially function). Specifically, we consider the mesh introduced in Section 2 with a domain length $L = 5 \mu\text{m}$ and $N = 100$ biological cells. The membrane model is described in Section 3.3 and notably includes homeostatic mechanisms. We further apply the stimulus current (16) and consider two different stimuli with periods $T_{\text{stim}} = 1 \text{ s}$ and $T_{\text{stim}} = 20$, which correspond to firing frequencies of 1 and 50 Hz, respectively. The stimulus current is applied on all mesh facets of the axon where $x \in (1.15, 1.25) \mu\text{m}$. The tissue domain is illustrated in Figure 8.

5.1 Membrane potentials and ion concentrations develop over different time scales during low neuronal activity

We start by analyzing the temporal dynamics of the system during a low firing frequency of 1 Hz over a period of 250 ms. We observe that an action potential fires at the onset of the simulation as a result of the stimulus current applied to the axon (Figure 9A). After the action potential, the membrane potential returns to a resting state at -72.5 mV , which is a 1.4% change from the initial state of -71.5 mV (Figure 9A). Meanwhile, the glial membrane potential initially increases rapidly during the action potential, by up to 0.6 mV from the initial value of -85 mV , before it steadily decreases over time reaching -84.6 mV at 250 ms (Figure 9B).

The action potential initiates rapid, coupled ionic shifts in both the intracellular and extracellular compartments. The neuronal Na^+ and K^+ concentrations respectively increase and decrease by approximately 4 mM during the action potential, before the concentrations slowly go back toward baseline levels as the homeostatic mechanisms (pumps, co-transporters and glial uptake) are activated. We observe that the neuronal Cl^- concentration rapidly increases as the neuron depolarizes, and decreases as the neuron

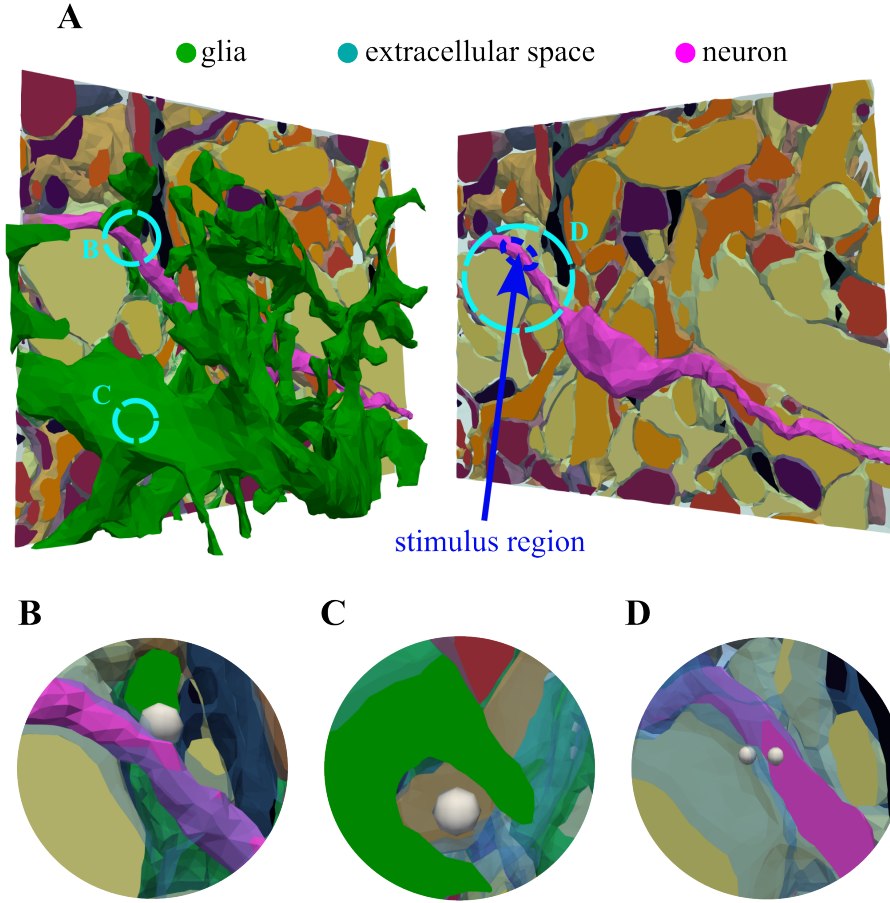


Fig. 8: **A.** Illustration of the computational mesh with $L = 5 \mu\text{m}$ and $N = 100$ with an astrocyte (green) partly wrapping around the stimulated axon (pink). The dashed blue ellipse indicates the stimulus region. The extracellular space is colored opaque light blue. All other colored structures are biological cells, with a unique color for every unique cell. **B.** Gray spherical glyph denoting point where glial intracellular concentrations are measured. **C.** Gray spherical glyph denoting point where distal extracellular concentrations are measured. **D.** Gray spherical glyphs denoting points where proximal extracellular concentrations (left) and neuronal intracellular concentrations (right) are measured.

repolarizes. Moreover, the Cl^- concentration drops below the initial state, indicating a total loss of neuronal Cl^- . Note that the changes in Cl^- are two orders of magnitude smaller than those observed for Na^+ and K^+ (Figure 9C).

In the extracellular space proximal to the stimulated region, all ion concentrations change abruptly when the stimulus current is applied (Figure 9D). In contrast to the neuronal concentrations, the shifts in the extracellular concentrations are of similar magnitude for all species. After the action potential is fired, both extracellular Na^+ and Cl^- concentrations proximal to the stimulated neuron settle at elevated values (around 1 mM higher than the initial concentrations). The extracellular K^+ concentration increases during the action potential, before decreasing as the homeostatic mechanism are activated, and is still decreasing at the end of the simulation. Distal to the neuron, the extracellular Na^+ and Cl^- concentrations are decreased by 0.017 and 0.012 mM, respectively, an order of magnitude less than the shifts of these ions proximal to the neuron. The distal K^+ concentration behaves similar to the proximal concentration, but the increase from the initial K^+ concentration to the peak concentration value in the distal point is half of that observed in the proximal point (Figure 9D).

The glial ion concentrations develop steadily over time throughout the entire simulation, with a decreasing Na^+ concentration while K^+ and Cl^- concentrations increase (Figure 9E). The ion concentration changes of the three species are similar in magnitude; at the end of the simulation, the Na^+ concentration has decreased by 0.026 mM, while K^+ and Cl^- concentrations have increased by 0.055 and 0.029 mM, respectively. In general, the ion concentrations stabilize over a much slower time scale than the membrane potentials. Both the membrane potentials and the concentrations approach a different set of steady-state values than the initial conditions (Figure 9C–E).

5.2 Sustained high-frequency firing induces a burst-firing mode

During high-frequency firing, where the axon is stimulated at a frequency of 50 Hz, the neuron initially fires a train of action potentials for approximately 400 ms (Figure 10A). At $t = 400$ ms, the neuron transitions into a new firing mode, characterized by bursts of two action potentials separated by silent periods that last around 180 ms. We observe that the amplitude of the membrane depolarization decreases over the first 400 ms; the initial AP peaks at 65 mV, while the last AP before the neuron transitions into a new firing mode peaks at less than 28 mV. We further observe an alteration of the hyperpolarization phase for each AP during the initial firing phase. Correspondingly, the glial membrane potential exhibits a slow, gradual depolarization over the 1000 ms simulation time, overlaid with small, rapid oscillations corresponding to the neuronal APs (Figure 10B). Notably, the initial AP depolarizes the glial membrane more heavily than the following APs.

The transition in neuronal firing pattern is underpinned by significant ionic shifts in both the intracellular and extracellular compartments. We observe that the neuronal Na^+ concentration increases rapidly while the K^+ concentration decreases rapidly during the initial firing phase. Both concentrations change by almost 40 mM during the sustained train of APs in the first 400 ms of the simulation. Following the transition to the burst-

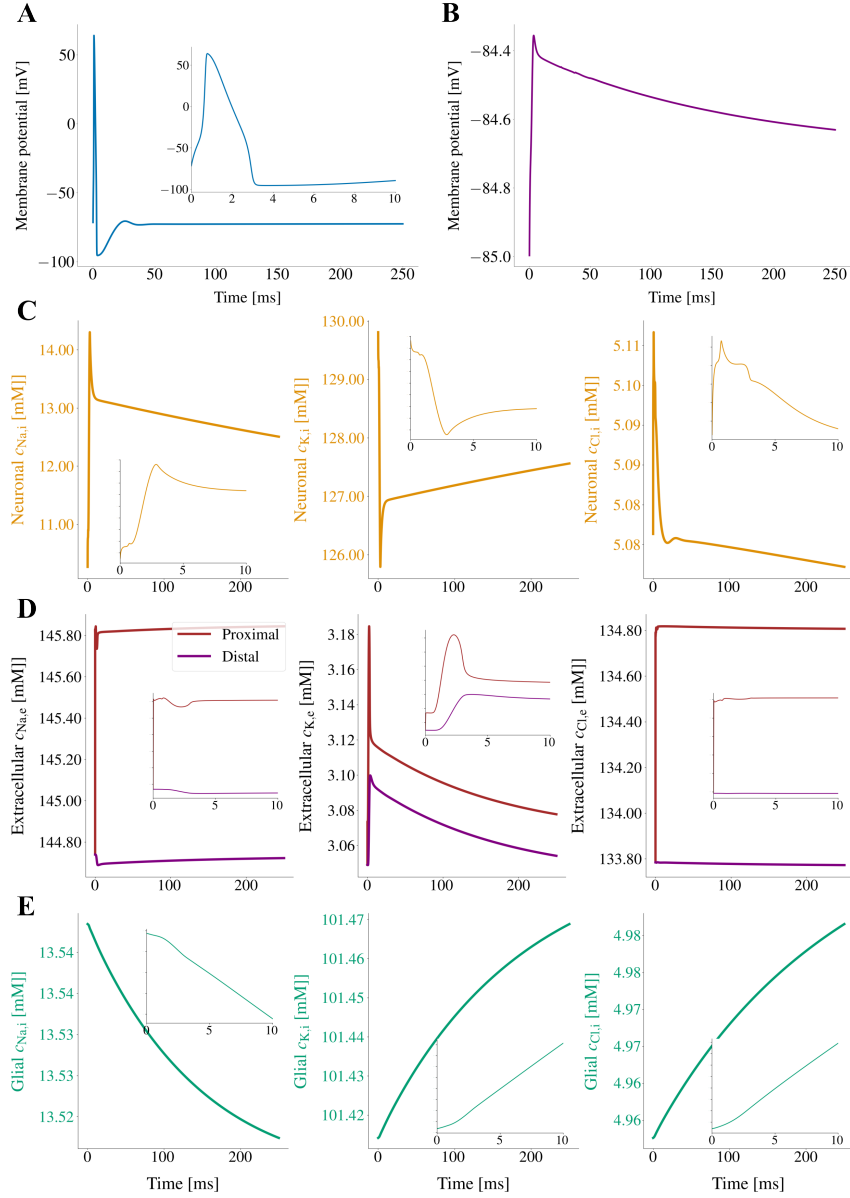


Fig. 9: Neuronal membrane potential (A), glial membrane potential (B), neuronal ion concentrations (C), extracellular ion concentrations (D) and glial ion concentrations (E) when simulating stimulation of an axon at a physiological frequency of 1 Hz on the $L = 5 \mu\text{m}$ mouse visual cortex mesh with $N = 100$ biological cells. The insets show the graphs during the first 10 ms. The insets have separate axes limits for the ICS and ECS concentrations (like in the original plots). In panel C, proximal and distal refer to the ECS points shown in Figure 8D and C, respectively.

firing mode, the ion concentration trends reverse during the silenced periods, indicating that the homeostatic mechanisms are activated. The neuronal Cl^- concentration displays significant oscillations, peaking near the onset of the second firing phase (Figure 10C). The Cl^- concentration changes are two orders of magnitude smaller than Na^+ and K^+ concentration changes.

We further observe that the extracellular K^+ concentration increases rapidly during the initial firing phase, reaching a peak of approximately 3.40 mM and 3.33 mM in the proximal and distal points, respectively, before decreasing (with notable peaks during the bursts) in the second firing phase (Figure 10D). The extracellular Na^+ and Cl^- concentrations decrease consistently over the simulation period in the distal point, whereas in the proximal point both concentrations increase rapidly at the onset of the simulation before Na^+ slowly increases while Cl^- decreases.

In contrast to the spiking behavior observed in the neuron and the ECS, the glial ion concentrations change gradually and more smoothly over time during both the AP train and the burst-firing mode (Figure 10E). The Na^+ concentration decreases, while both K^+ and Cl^- increase. The rates of change decrease after the onset of the burst-firing mode, and all ion concentrations appear to saturate.

5.3 Cellular morphology determines how ion concentrations and electric potentials develop in space during neuronal activity

We now turn to the spatial distribution of ion concentrations and electric potentials. During firing of a single action potential, the extracellular K^+ concentration is fairly constant in the initial phase when the membrane potential rises (Figure 11A, B). Subsequent to the membrane potential peak, the increase in extracellular K^+ spreads through the extracellular space fast as the voltage-gate K^+ channels open (Figure 11C–E). During the action potential, the extracellular Na^+ concentration decreases gradually proximal to the neuron, with less notable changes in distal locations (Figure 11F–J).

There are notable local differences in the neuronal concentrations, with distinctly greater K^+ and lower Na^+ concentrations in the axonal varicosity (widened section) of the stimulated neuron after the action potential, compared to the slender structures of the axon. (Figure 11E, J). At time $t = 2.5$ ms, the Na^+ concentration is 2-3 mM greater in the slender structures than in the varicosity.

At a given time instant, there are also small spatial differences in the electric potentials in the stimulated neuron and the extracellular space. After the peak of the first action potential at time $t = 2.5$ ms, the extracellular potential ϕ_e is most negative close to the neuron, especially near the axonal varicosity (Figure 12A). The intracellular potential ϕ_i is also lowest on the membrane of the varicosity. After $t = 1000$ ms, subsequent to sustained stimulus with a frequency of 50 Hz, the situation is reversed for the extracellular potential (Figure 12B). Now, the potential is less negative close to the neuron. Also, the maximum spatial differences in ϕ_e at time $t = 1000$ ms are around 0.14 mV in magnitude, more than an order greater than the maximum difference of 0.008 mV at $t = 2.5$ ms.

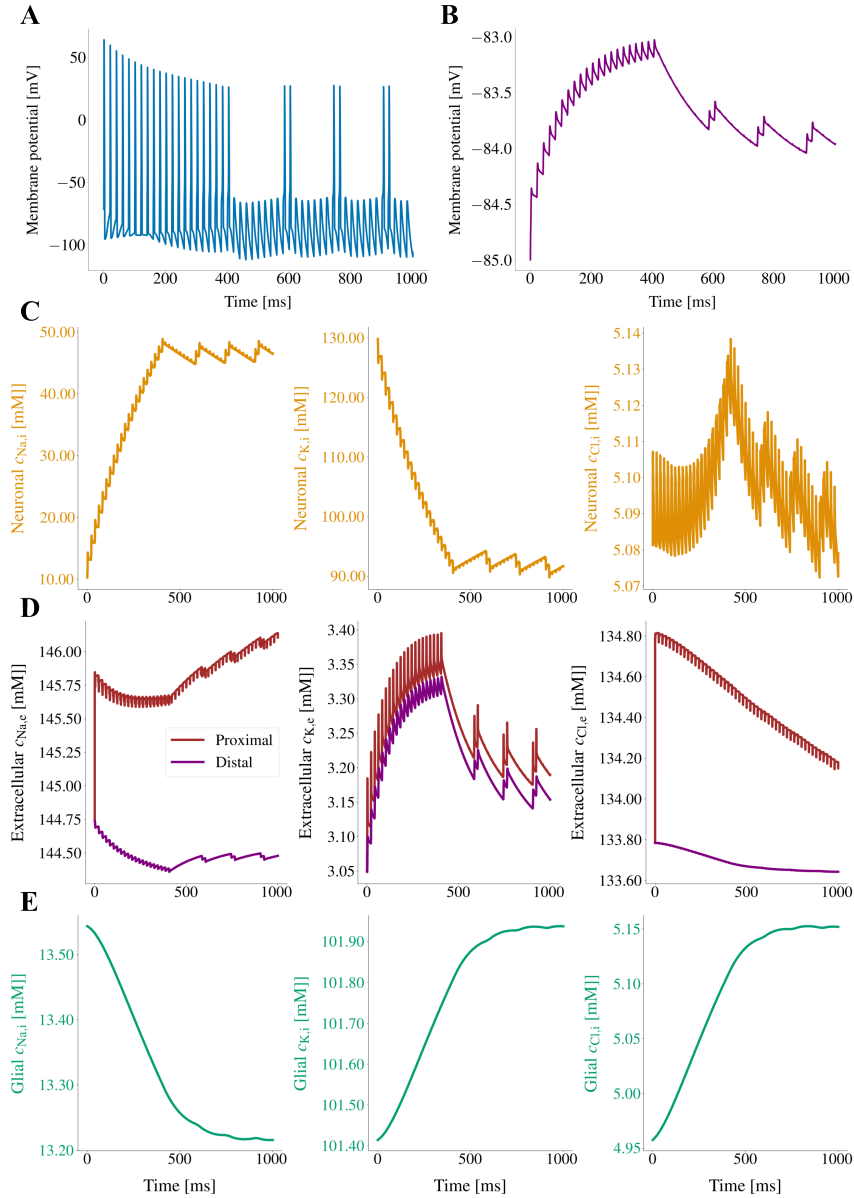


Fig. 10: Neuronal membrane potential (A), glial membrane potential (B), neuronal ion concentrations (C), extracellular ion concentrations (D) and glial ion concentrations (E) when simulating stimulation of an axon at a frequency of 50 Hz on the $L = 5 \mu\text{m}$ mouse visual cortex mesh with $N = 100$ biological cells. The insets show the graphs during the first 10 ms. The insets have separate axes limits for the ICS and ECS concentrations (like in the original plots). In panel C, proximal and distal refer to the ECS points shown in Figure 8D and C, respectively.

In the astrocyte wrapping around the stimulated neuron, the intracellular K^+ at $t = 2.5$ ms has increased most close to the neuron and in slender structures (Figure 13A). The spatial variation in glial K^+ concentration is as low as 0.002 mM, whereas in the extracellular space, the concentrations differ by around 0.14 mM. Later at $t = 1000$ ms, the intracellular K^+ differs by around 0.016 mM (Figure 13B). The extracellular K^+ concentration is essentially uniform in space, except for locally elevated values in the stimulus region (Figure 13B inset).

6 Discussion and outlook

We have presented a computational framework for simulation of electrodiffusion in cellular geometries based on a finite element method for the KNP-EMI equations. We have also demonstrated a pipeline for generating realistic computational meshes from electron microscopy data that represents dense reconstructions of cerebral tissue. Using such a geometry of mouse visual cortex tissue, we applied our computational framework to simulate electrodiffusive dynamics during neuronal activity at low- and high-frequency firing. The results clearly show that morphology and shape affect the electrodiffusive dynamics.

We also reported on the characteristics of dense reconstructions of cerebral tissue by generating a series of meshes with varying domain sizes and number of biological cells. We found that the number of membrane points in the geometries are high compared to the total number of points, especially for geometries with a high number of biological cells. This poses a challenge for strongly coupled problems such as the electrodiffusive KNP-EMI equations, with ion concentrations and electric potentials developing over varying temporal and spatial scales. Since theory based on spectral analysis and simulations based on the EMI equations suggest that the preconditioner we employ will struggle for a high ratio of membrane points [6, 7, 5], we assessed how the iterative solver performs in this setting. For the smaller geometries, the solver performed consistently in spite of high membrane-point ratios, but performance deteriorated with increasingly complex geometries. It would be interesting to investigate how PDE splitting strategies, contrasting our monolithic approach, would perform on these geometries.

In terms of limitations, two important considerations are the following. First, there are uncertainties in the membrane mechanism parameters that are adopted from simpler models. This calls for validation by comparing simulations with physical experiments. Another alternative is an uncertainty quantification study. Second, the geometries used have narrow extracellular structures where the distance separating two cells may approach the limit of the electroneutrality assumption in the KNP equations. The KNP approximation has shown to be excellent on the micrometer scale [23]. When modeling dynamics very close to the cellular membranes at the nanometer scale, the small spatial and temporal scales require solving a Poisson equation for the electric potentials, forming the Poisson-Nernst-Planck (PNP) equations to fully incorporate the rapid dynamics [31]. A comparison study of the two approaches (KNP and PNP) on the mouse visual cortex geometries could shed light on this matter.

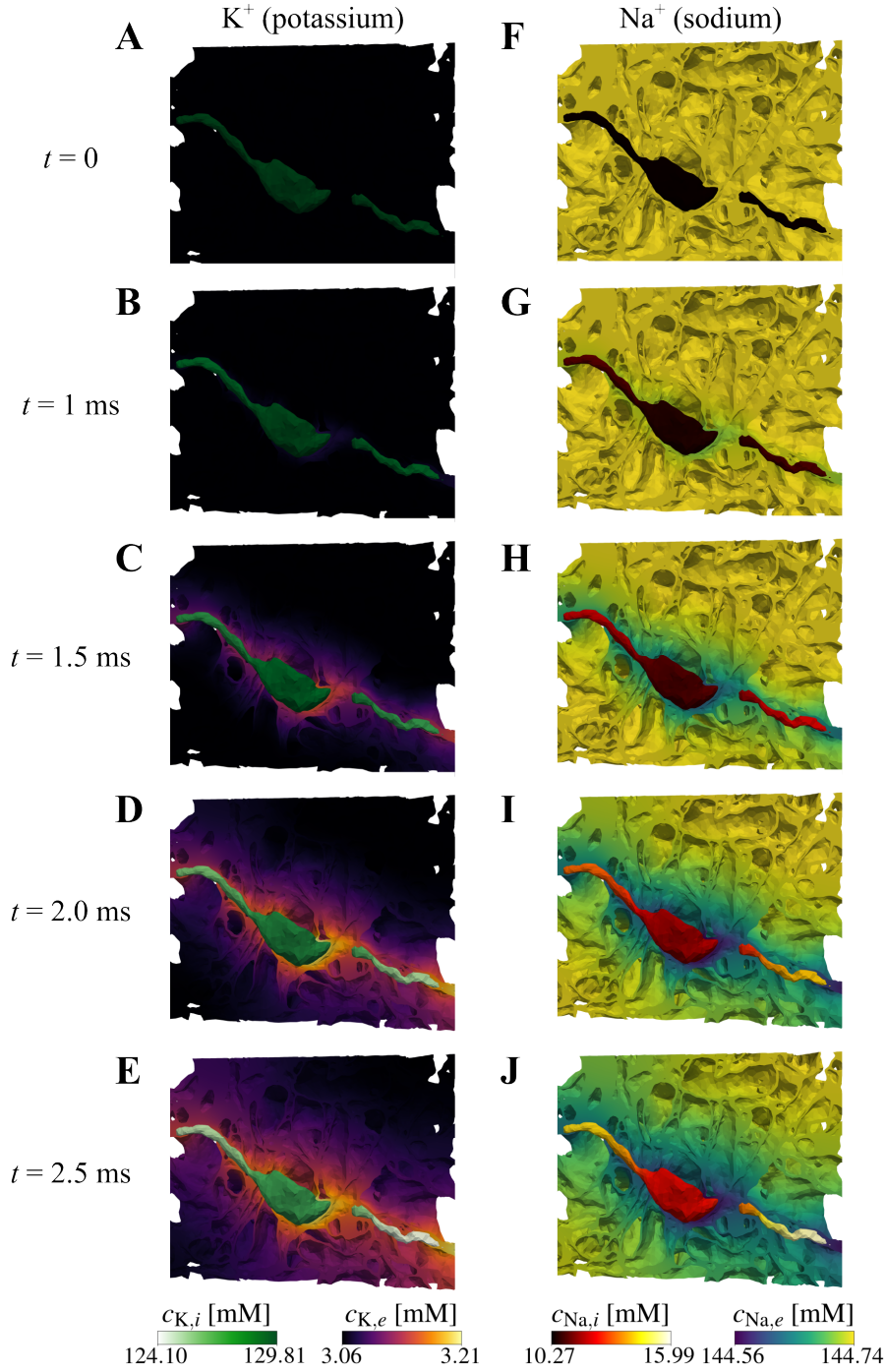


Fig. 11: Potassium (A–E) and sodium (F–J) concentrations in the stimulated neuron and the extracellular space over time when simulating the firing of an action potential using the $L = 5 \mu\text{m}$, $N = 100$ mouse visual cortex geometry. The ECS is clipped and no other cells than the stimulated neuron are shown.

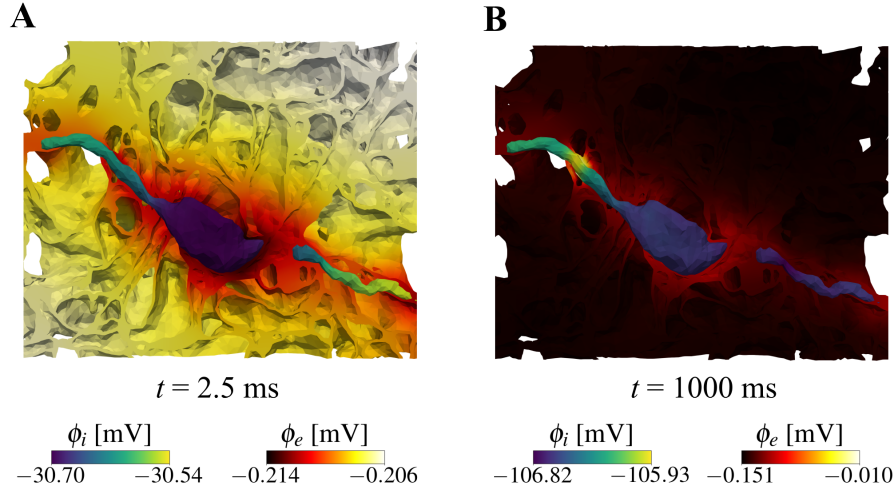


Fig. 12: Electric potentials in the stimulated neuron and the extracellular space at times $t = 2.5$ ms (A) and $t = 1000$ ms (B). The ECS is clipped and the only cell shown is the neuron that is stimulated. Note the individual colorbars for each of the subpanels.

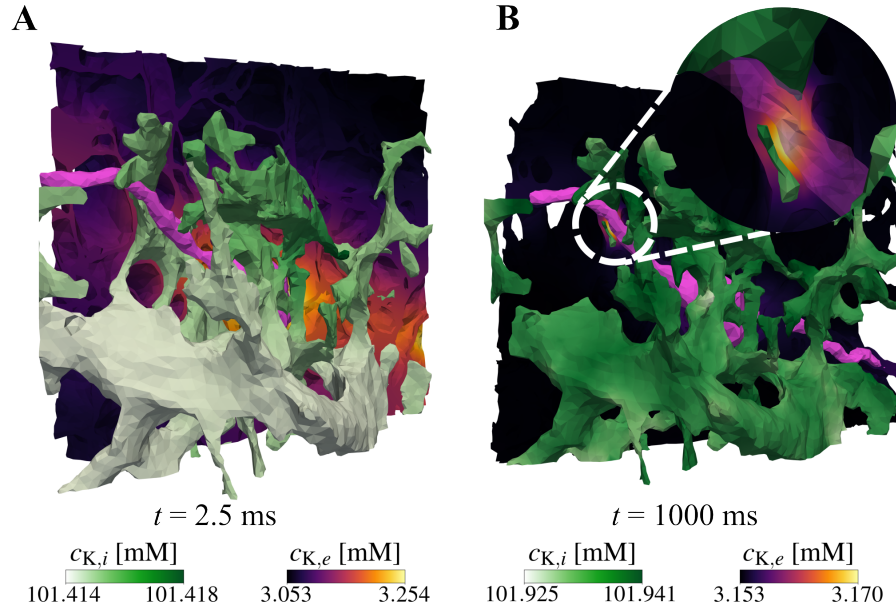


Fig. 13: Potassium concentrations in an astrocyte (glial cell) and the extracellular space at times $t = 2.5$ ms (A) and $t = 1000$ ms (B) when simulating a neuron (pink) with a frequency of 50 Hz. The ECS is clipped. Note the individual colorbars for each of the subpanels.

Altogether, the content of this chapter exemplifies that scientific computing has developed to the point where numerical solutions of partial differential equations on realistic brain tissue geometries are feasible. There are however still unresolved questions, but future works can hopefully continue to push the boundaries of computational neuroscience studies even further.

Acknowledgements We are grateful to Pietro Benedusi for interesting discussions and for providing input to Figure 5. The research presented in this chapter has benefited from the Experimental Infrastructure for Exploration of Exascale Computing (eX3), a computational infrastructure that is financially supported by the Research Council of Norway under contract #270053. G. T. E. acknowledges funding from the European Union Horizon 2020 Research and Innovation Programme under Grant Agreement No. 101147319 (EBRAINS 2.0). M. C. acknowledges funding from the European Research Council under grant No. 101141807 (aCleanBrain). M.E.R. acknowledges support from Stiftelsen Kristian Gerhard Jebsen via the K. G. Jebsen Centre for Brain Fluid Research and Wellcome via Award 313298/Z/24/Z (Next-generation simulation and learning in imaging-based biomedicine).

Competing Interests The authors have no conflicts of interest to declare that are relevant to the content of this chapter.

References

1. Agudelo-Toro, A., Neef, A.: Computationally efficient simulation of electrical activity at cell membranes interacting with self-generated and externally imposed electric fields. *Journal of neural engineering* **10**(2), 026019 (2013)
2. Aidley, D.J.: *The physiology of excitable cells*. Cambridge University Press (1998)
3. Aitken, P., Somjen, G.: The sources of extracellular potassium accumulation in the ca1 region of hippocampal slices. *Brain research* **369**(1-2), 163–167 (1986)
4. Baratta, I.A., Dean, J.P., Dokken, J.S., Habera, M., Hale, J.S., Richardson, C.N., Rognes, M.E., Scroggs, M.W., Sime, N., Wells, G.N.: DOLFINx: The next generation FEniCS problem solving environment (2023). DOI 10.5281/zenodo.10447666
5. Benedusi, P., Ellingsrud, A.J., Herlyng, H., Rognes, M.E.: Scalable Approximation and Solvers for Ionic Electrodiffusion in Cellular Geometries. *SIAM Journal on Scientific Computing* **46**(5), B725–B751 (2024). DOI 10.1137/24M1644717. URL <https://doi.org/10.1137/24M1644717>
6. Benedusi, P., Ferrari, P., Causemann, M., Serra-Capizzano, S.: Dense cell-by-cell systems of PDEs: approximation, spectral analysis, and preconditioning. *arXiv preprint arXiv:2409.13432* (2024)
7. Benedusi, P., Ferrari, P., Rognes, M.E., Serra-Capizzano, S.: Modeling excitable cells with the EMI equations: Spectral analysis and iterative solution strategy. *Journal of Scientific Computing* **98**(3), 58 (2024)
8. Betzel, R.F., Bassett, D.S.: Multi-scale brain networks. *Neuroimage* **160**, 73–83 (2017)
9. Causemann, M.: Emi-meshing: High-quality extracellular-membrane- intracellular meshes of the mouse visual cortex (2024). DOI 10.5281/zenodo.13373950. URL <https://doi.org/10.5281/zenodo.13373950>
10. Chen, A.B., Duque, M., Rymbek, A., Dhanasekar, M., Wang, V.M., Mi, X., Tocquer, L., Narayan, S., Legorreta, E.M., Eddison, M., Yu, G., Wyart, C., Prober, D.A., Engert, F., Ahrens, M.B.: Norepinephrine changes behavioral state through astroglial purinergic signaling. *Science* **388**(6748), 769–775 (2025). DOI 10.1126/science.adq5233. URL <https://www.science.org/doi/abs/10.1126/science.adq5233>
11. Chen, K.C., Nicholson, C.: Spatial buffering of potassium ions in brain extracellular space. *Biophysical journal* **78**(6), 2776–2797 (2000)

12. Consortium, T.M.: Functional connectomics spanning multiple areas of mouse visual cortex. *Nature* **640**(8058), 435–447 (2025)
13. D, P., GJ, A., D, F.: *Neuroscience*, 2nd edn. Sunderland (MA): Sinauer Associates (2001)
14. De Pittà, M., Berry, H.: *Computational glioscience*. Springer (2019)
15. Einevoll, G.T.: Mathematical modeling of neural activity. In: *Dynamics of complex interconnected systems: Networks and bioprocesses*, pp. 127–145. Springer (2006)
16. Ellingsrud, A.J., Benedusi, P., Kuchta, M.: A splitting, discontinuous Galerkin solver for the cell-by-cell electroneutral Nernst–Planck framework. *SIAM Journal on Scientific Computing* **47**(2), B477–B504 (2025)
17. Ellingsrud, A.J., Daversin-Catty, C., Rognes, M.E.: A Cell-Based Model for Ionic Electrodiffusion in Excitable Tissue. *Modeling Excitable Tissue: The EMI Framework* **7**, 14–27 (2021)
18. Ellingsrud, A.J., Solbrå, A., Einevoll, G.T., Hånes, G., Rognes, M.E.: Finite element simulation of ionic electrodiffusion in cellular geometries. *Frontiers in neuroinformatics* **14**, 11 (2020)
19. Fu, X.M., Liu, Y., Guo, B.: Computing locally injective mappings by advanced mips. *ACM Transactions on Graphics (TOG)* **34**(4), 1–12 (2015)
20. Glaser, A., Chandrashekar, J., Vasquez, S., Arshadi, C., Javeri, R., Ouellette, N., Jiang, X., Baka, J., Kovacs, G., Woodard, M., et al.: Expansion-assisted selective plane illumination microscopy for nanoscale imaging of centimeter-scale tissues. *Elife* **12**, RP91979 (2025)
21. Guttenplan, K.A., Maxwell, I., Santos, E., Borchardt, L.A., Manzo, E., Abalde-Atristain, L., Kim, R.D., Freeman, M.R.: GPCR signaling gates astrocyte responsiveness to neurotransmitters and control of neuronal activity. *Science* **388**(6748), 763–768 (2025). DOI 10.1126/science.adq5729. URL <https://www.science.org/doi/abs/10.1126/science.adq5729>
22. Haase, R., Rajasekhar, P., Lambert, T., grahamross123, Nunez-Iglesias, J., Lachie, Caporal, C., Avenel, C., ENicolay, Elissavet, Korten, T.: *clesperanto/pyclesperanto_prototype*. https://github.com/clEsperanto/pyclesperanto_prototype (2025). URL https://github.com/clEsperanto/pyclesperanto_prototype
23. Hånes, G., Mäki-Marttunen, T., Keller, D., Pettersen, K.H., Andreassen, O.A., Einevoll, G.T.: Effect of ionic diffusion on extracellular potentials in neural tissue. *PLoS computational biology* **12**(11), e1005193 (2016)
24. Hånes, G., Ness, T.V., Næss, S., Hagen, E., Pettersen, K.H., Einevoll, G.T.: *Electric brain signals: foundations and applications of biophysical modeling*. Cambridge University Press (2024)
25. Hånes, G., Østby, I., Pettersen, K.H., Omholt, S.W., Einevoll, G.T.: Electrodiffusive Model for Astrocytic and Neuronal Ion Concentration Dynamics. *PLOS Computational Biology* **9**(12), 1–16 (2013). DOI 10.1371/journal.pcbi.1003386. URL <https://doi.org/10.1371/journal.pcbi.1003386>
26. Häusser, M.: The Hodgkin-Huxley theory of the action potential. *Nature neuroscience* **3**(11), 1165–1165 (2000)
27. Hille, B.: *Ion channels of excitable membranes* (2001). Sinauer, Sunderland, MA
28. Hodgkin, A.L., Huxley, A.F.: A quantitative description of membrane current and its application to conduction and excitation in nerve. *The Journal of physiology* **117**(4), 500 (1952)
29. Hu, Y., Schneider, T., Wang, B., Zorin, D., Panozzo, D.: Fast tetrahedral meshing in the wild. *ACM Trans. Graph.* **39**(4) (2020). DOI 10.1145/3386569.3392385
30. *hypre*: High performance preconditioners. <https://llnl.gov/casc/hypre>, <https://github.com/hypre-space/hypre>
31. Jæger, K.H., Ivanovic, E., Kucera, J.P., Tveito, A.: Nano-scale solution of the Poisson-Nernst-Planck (PNP) equations in a fraction of two neighboring cells reveals the magnitude of intercellular electrochemical waves. *PLoS computational biology* **19**(2), e1010895 (2023)
32. Johnson, C.: *Numerical solution of partial differential equations by the finite element method*. Courier Corporation (2009)
33. Kager, H., Wadman, W.J., Somjen, G.G.: Simulated seizures and spreading depression in a neuron model incorporating interstitial space and ion concentrations. *Journal of neurophysiology* **84**(1), 495–512 (2000)
34. Kandel, E.R., Schwartz, J.H., Jessell, T.M., Siegelbaum, S., Hudspeth, A.J., Mack, S., et al.: *Principles of neural science*, vol. 4. McGraw-hill New York (2000)
35. Kaszynski, A.: *pyvista/pyacvd*. <https://github.com/pyvista/pyacvd> (2025). URL <https://github.com/pyvista/pyacvd>

36. Kofuji, P., Newman, E.: Potassium buffering in the central nervous system. *Neuroscience* **129**(4), 1043–1054 (2004)
37. Laboratory, S.R.: Experimental Infrastructure for Exploration of Exascale Computing. URL <https://www.ex3.simula.no/>. Accessed: 30.07.2025
38. Lee, W.C.A., Huang, H., Feng, G., Sanes, J.R., Brown, E.N., So, P.T., Nedivi, E.: Dynamic remodeling of dendritic arbors in gabaergic interneurons of adult visual cortex. *PLoS biology* **4**(2), e29 (2006)
39. Lefton, K.B., Wu, Y., Dai, Y., Okuda, T., Zhang, Y., Yen, A., Rurak, G.M., Walsh, S., Manno, R., Myagmar, B.E., Dougherty, J.D., Samineni, V.K., Simpson, P.C., Papouin, T.: Norepinephrine signals through astrocytes to modulate synapses. *Science* **388**(6748), 776–783 (2025). DOI 10.1126/science.adq5480. URL <https://www.science.org/doi/abs/10.1126/science.adq5480>
40. Lopreore, C.L., Bartol, T.M., Coggan, J.S., Keller, D.X., Sosinsky, G.E., Ellisman, M.H., Sejnowski, T.J.: Computational modeling of three-dimensional electrodiffusion in biological systems: application to the node of Ranvier. *Biophysical journal* **95**(6), 2624–2635 (2008)
41. Lu, B., Holst, M.J., McCammon, J.A., Zhou, Y.: Poisson–nernst–planck equations for simulating biomolecular diffusion–reaction processes i: Finite element solutions. *Journal of computational physics* **229**(19), 6979–6994 (2010)
42. MICrONS Consortium: Neuroglancer. URL <https://www.microns-explorer.org/ngl-instructions>. Accessed: 11.08.2025
43. Mori, Y., Peskin, C.: A numerical method for cellular electrophysiology based on the electrodiffusion equations with internal boundary conditions at membranes. *Communications in Applied Mathematics and Computational Science* **4**(1), 85–134 (2009)
44. Nicholson, C., Ten Bruggencate, G., Stockle, H., Steinberg, R.: Calcium and potassium changes in extracellular microenvironment of cat cerebellar cortex. *Journal of neurophysiology* **41**(4), 1026–1039 (1978)
45. Østby, I., Øyehaug, L., Einevoll, G.T., Nagelhus, E.A., Plahte, E., Zeuthen, T., Lloyd, C.M., Ottersen, O.P., Omholt, S.W.: Astrocytic mechanisms explaining neural-activity-induced shrinkage of extraneuronal space. *PLoS computational biology* **5**(1), e1000272 (2009)
46. Øyehaug, L.: Slow ion concentration oscillations and multiple states in neuron–glia interaction—insights gained from reduced mathematical models. *Frontiers in Network Physiology* **3**, 1189118 (2023)
47. Øyehaug, L., Østby, I., Lloyd, C.M., Omholt, S.W., Einevoll, G.T.: Dependence of spontaneous neuronal firing and depolarisation block on astroglial membrane transport mechanisms. *Journal of computational neuroscience* **32**(1), 147–165 (2012)
48. Pods, J., Schöнке, J., Bastian, P.: Electrodiffusion models of neurons and extracellular space using the poisson–nernst–planck equations—numerical simulation of the intra-and extracellular potential for an axon model. *Biophysical journal* **105**(1), 242–254 (2013)
49. Rasmussen, R., O'Donnell, J., Ding, F., Nedergaard, M.: Interstitial ions: A key regulator of state-dependent neural activity? *Progress in Neurobiology* **193** (2020). DOI 10.1016/j.pneurobio.2020.101802
50. Roache, P.J.: Code Verification by the Method of Manufactured Solutions. *Journal of Fluids Engineering* **124**(1), 4–10 (2001). URL <https://doi.org/10.1115/1.1436090>
51. Roy, T., Andrej, J., Beck, V.A.: A scalable DG solver for the electroneutral Nernst–Planck equations. *Journal of Computational Physics* **475**, 111859 (2023)
52. Rush, S., Larsen, H.: A practical algorithm for solving dynamic membrane equations. *IEEE Transactions on Biomedical Engineering* pp. 389–392 (2007)
53. Saad, Y., Schultz, M.H.: GMRES: A generalized minimal residual algorithm for solving non-symmetric linear systems. *SIAM Journal on scientific and statistical computing* **7**(3), 856–869 (1986)
54. Sætra, M.J., Einevoll, G.T., Haldnes, G.: An electrodiffusive, ion conserving Pinsky–Rinzel model with homeostatic mechanisms. *PLOS Computational Biology* **16**(4), e1007661 (2020)
55. Sætra, M.J., Einevoll, G.T., Haldnes, G.: An electrodiffusive neuron–extracellular–glia model for exploring the genesis of slow potentials in the brain. *PLoS Computational Biology* **17**(7), e1008143 (2021)

56. Sætra, M.J., Ellingsrud, A.J., Rognes, M.E.: Neural activity induces strongly coupled electro-chemo-mechanical interactions and fluid flow in astrocyte networks and extracellular space—a computational study. *PLoS Computational Biology* **19**(7), e1010996 (2023)
57. Sætra, M.J., Mori, Y.: An electrodiffusive network model with multicompartmental neurons and synaptic connections. *PLOS Computational Biology* **20**(11), e1012114 (2024)
58. Solbrå, A., Bergersen, A.W., van den Brink, J., Malthe-Sørenssen, A., Einevoll, G.T., Hånes, G.: A Kirchhoff-Nernst-Planck framework for modeling large scale extracellular electrodiffusion surrounding morphologically detailed neurons. *PLoS computational biology* **14**(10), e1006510 (2018)
59. Somjen, G.G.: Ion regulation in the brain: implications for pathophysiology. *The neuroscientist* **8**(3), 254–267 (2002)
60. Steinmetz, J.D., Seeher, K.M., Schiess, N., Nichols, E., Cao, B., Servili, C., Cavallera, V., Cousin, E., Hagins, H., Moberg, M.E., et al.: Global, regional, and national burden of disorders affecting the nervous system, 1990–2021: a systematic analysis for the Global Burden of Disease Study 2021. *The Lancet Neurology* **23**(4), 344–381 (2024)
61. Sterratt, D., Graham, B., Gillies, A., Einevoll, G., Willshaw, D.: Principles of computational modelling in neuroscience. Cambridge university press (2023)
62. Sullivan, B., Kaszynski, A.: PyVista: 3D plotting and mesh analysis through a streamlined interface for the Visualization Toolkit (VTK). *Journal of Open Source Software* **4**(37), 1450 (2019). DOI 10.21105/joss.01450. URL <https://doi.org/10.21105/joss.01450>
63. Tavakoli, M.R., Lyudchik, J., Januszewski, M., Vistunou, V., Agudelo Dueñas, N., Vorlauffer, J., Sommer, C., Kreuzinger, C., Oliveira, B., Cenameri, A., et al.: Light-microscopy-based connectomic reconstruction of mammalian brain tissue. *Nature* pp. 1–13 (2025)
64. Tveito, A., Jæger, K.H., Lines, G.T., Paszkowski, Ł., Sundnes, J., Edwards, A.G., Mäki-Marttunen, T., Hånes, G., Einevoll, G.T.: An evaluation of the accuracy of classical models for computing the membrane potential and extracellular potential for neurons. *Frontiers in computational neuroscience* **11**, 27 (2017)
65. Tveito, A., Mardal, K.A., Rognes, M.E.: Modeling excitable tissue: The EMI framework. Springer Nature (2021)
66. Untiet, V.: Astrocytic chloride regulates brain function in health and disease. *Cell Calcium* **118**, 102855 (2024)
67. Utzschneider, D., Kocsis, J., Devor, M.: Mutual excitation among dorsal root ganglion neurons in the rat. *Neuroscience letters* **146**(1), 53–56 (1992)
68. Walz, W.: Role of astrocytes in the clearance of excess extracellular potassium. *Neurochemistry international* **36**(4-5), 291–300 (2000)
69. Wei, Y., Ullah, G., Schiff, S.J.: Unification of neuronal spikes, seizures, and spreading depression. *Journal of Neuroscience* **34**(35), 11733–11743 (2014)
70. Yang, U.M., et al.: BoomerAMG: A parallel algebraic multigrid solver and preconditioner. *Applied Numerical Mathematics* **41**(1), 155–177 (2002)
71. Yen, C., Lin, C.L., Chiang, M.C.: Exploring the frontiers of neuroimaging: a review of recent advances in understanding brain functioning and disorders. *Life* **13**(7), 1472 (2023)

Appendix

Numerical verification of the iterative numerical method with idealized geometries

Here, we verify spatial convergence properties of the iterative numerical method by performing a convergence study with two idealized problems. The first problem considers the domain $\Omega = [0, 1]^2 \mu\text{m}^2$ with boundary $\partial\Omega$, with an inner square $\Omega_i = [0.25, 0.75]^2 \mu\text{m}^2$ as intracellular space and $\Omega_e = \Omega \setminus \Omega_i$ as extracellular space. The interface that separates Ω_i and Ω_e is the cellular membrane Γ . The second problem is similar, and considers the cube $\Omega = [0, 1]^3 \mu\text{m}^3$ with an inner cube $\Omega_i = [0.25, 0.75]^3 \mu\text{m}^3$ as intracellular space and $\Omega_e = \Omega \setminus \Omega_i$ as extracellular space. The cellular membrane Γ is also here defined as the interface between Ω_i and Ω_e . The two problem domains are meshed with triangles and tetrahedra with mesh edge lengths h . To assess convergence, we consider a series of increasingly refined meshes. The coarsest mesh edge length of the two problems is denoted h_0 .

Convergence is verified by manufacturing solutions for both problems [50]. The parameter values of R , F , T and C_m are all set to 1. We solve the problems for one timestep using $\Delta t = 1 \times 10^{-5}$, and compute the L^2 -error for the concentrations and potentials Tables 7 and 8. Although a priori error estimates for the KNP-EMI problem are not yet well-established, the convergence rate when using continuous Lagrange elements of order p to approximate a finite element solution is bounded from above by $p + 1$ [32]. We observe convergence rates of $p + 1$, both for the 2D and the 3D test problems.

Table 7: Error norms and convergence rates for the two-dimensional verification problem on meshes of increasing resolution characterized by the edge lengths h . The coarsest mesh has mesh edge length h_0 .

h/h_0	$\ c_{\text{Na},i} - c_{\text{Na},i,\text{exact}}\ _{L^2}$	$\ c_{\text{K},i} - c_{\text{K},i,\text{exact}}\ _{L^2}$	$\ c_{\text{Cl},i} - c_{\text{Cl},i,\text{exact}}\ _{L^2}$	$\ \phi_i - \phi_{i,\text{exact}}\ _{L^2}$
1	9.01×10^{-3} (–)	9.00×10^{-3} (–)	1.80×10^{-2} (–)	9.26×10^{-2} (–)
1/2	2.33×10^{-3} (1.95)	2.33×10^{-3} (1.95)	4.67×10^{-3} (1.95)	2.48×10^{-2} (1.90)
1/4	5.88×10^{-4} (1.99)	5.88×10^{-4} (1.99)	1.17×10^{-3} (1.99)	6.30×10^{-3} (1.98)
1/8	1.47×10^{-4} (2.00)	1.47×10^{-4} (2.00)	2.94×10^{-4} (2.00)	1.58×10^{-3} (2.00)
1/16	3.68×10^{-5} (2.00)	3.63×10^{-5} (2.02)	7.26×10^{-5} (2.02)	3.95×10^{-4} (2.00)
	$\ c_{\text{Na},e} - c_{\text{Na},e,\text{exact}}\ _{L^2}$	$\ c_{\text{K},e} - c_{\text{K},e,\text{exact}}\ _{L^2}$	$\ c_{\text{Cl},e} - c_{\text{Cl},e,\text{exact}}\ _{L^2}$	$\ \phi_e - \phi_{e,\text{exact}}\ _{L^2}$
1	3.12×10^{-2} (–)	1.04×10^{-2} (–)	4.16×10^{-2} (–)	6.13×10^{-2} (–)
1/2	8.08×10^{-3} (1.95)	2.69×10^{-3} (1.95)	1.08×10^{-3} (1.95)	1.67×10^{-2} (1.88)
1/4	2.04×10^{-3} (1.99)	6.79×10^{-4} (1.99)	2.72×10^{-3} (1.99)	4.25×10^{-3} (1.97)
1/8	5.09×10^{-4} (2.00)	1.70×10^{-4} (2.00)	6.78×10^{-4} (2.00)	1.07×10^{-3} (1.99)
1/16	1.26×10^{-4} (2.00)	4.19×10^{-5} (2.02)	1.68×10^{-4} (2.02)	2.68×10^{-4} (2.00)

Table 8: Error norms and convergence rates for the three-dimensional verification problem on meshes of increasing resolution characterized by the edge lengths h . The coarsest mesh has mesh edge length h_0 .

h/h_0	$\ c_{Na,i} - c_{Na,i,\text{exact}}\ _{L^2}$	$\ c_{K,i} - c_{K,i,\text{exact}}\ _{L^2}$	$\ c_{Cl,i} - c_{Cl,i,\text{exact}}\ _{L^2}$	$\ \phi_i - \phi_{i,\text{exact}}\ _{L^2}$
1	6.70×10^{-3} (–)	6.70×10^{-3} (–)	1.34×10^{-2} (–)	6.82×10^{-2} (–)
1/2	1.79×10^{-3} (1.90)	1.79×10^{-3} (1.90)	3.58×10^{-3} (1.90)	1.93×10^{-2} (1.82)
1/4	4.54×10^{-4} (1.98)	4.55×10^{-4} (1.98)	9.09×10^{-4} (1.98)	4.99×10^{-3} (1.95)
1/8	1.14×10^{-4} (2.00)	1.14×10^{-4} (2.00)	2.28×10^{-4} (2.00)	1.26×10^{-3} (1.99)
1/16	2.83×10^{-5} (2.01)	2.83×10^{-5} (2.01)	5.66×10^{-5} (2.01)	3.16×10^{-4} (2.00)
	$\ c_{Na,e} - c_{Na,e,\text{exact}}\ _{L^2}$	$\ c_{K,e} - c_{K,e,\text{exact}}\ _{L^2}$	$\ c_{Cl,e} - c_{Cl,e,\text{exact}}\ _{L^2}$	$\ \phi_e - \phi_{e,\text{exact}}\ _{L^2}$
1	3.55×10^{-2} (–)	1.12×10^{-2} (–)	4.73×10^{-2} (–)	6.74×10^{-2} (–)
1/2	9.47×10^{-3} (1.90)	3.16×10^{-3} (1.90)	1.26×10^{-3} (1.90)	1.96×10^{-2} (1.78)
1/4	2.41×10^{-3} (1.98)	8.02×10^{-4} (1.98)	3.21×10^{-3} (1.98)	5.11×10^{-3} (1.94)
1/8	6.03×10^{-4} (2.00)	2.01×10^{-4} (2.00)	8.04×10^{-4} (2.00)	1.29×10^{-3} (1.98)
1/16	1.50×10^{-4} (2.01)	4.99×10^{-5} (2.01)	2.00×10^{-4} (2.01)	3.24×10^{-4} (2.00)

Numerical verification with a realistic cerebral tissue geometry

With the spatial convergence properties verified on idealized geometries, we here verify that the numerical solution of the KNP-EMI model converges on the mouse visual cortex tissue mesh. We perform a convergence study by solving the KNP-EMI equations on the original $L = 5 \mu\text{m}$, $N = 100$ mesh (generated with EMI-Meshing as introduced in Section 2), and two uniformly refined versions of the mesh. We run a similar simulation as described in Section 5; an axon is stimulated with the stimulus current density defined in Equation (16) with $T_{\text{stim}} = 1$ s. The simulation is run for 800 timesteps with $\Delta t = 2.5 \times 10^{-5}$ to a final time of $T = 10$ ms. We evaluate the membrane potential in the point $\mathbf{x} = (1186, 3241, 3594)$ nm on the stimulated neuron. The neuronal intracellular sodium concentration, the extracellular potassium concentration proximal to the neuron, and the glial intracellular Cl^- concentration are all evaluated in the same points as described in Section 5, see Figure 8. The solutions obtained are similar to the results observed in Section 5, and the results agree well across the different mesh versions (Figure 14).

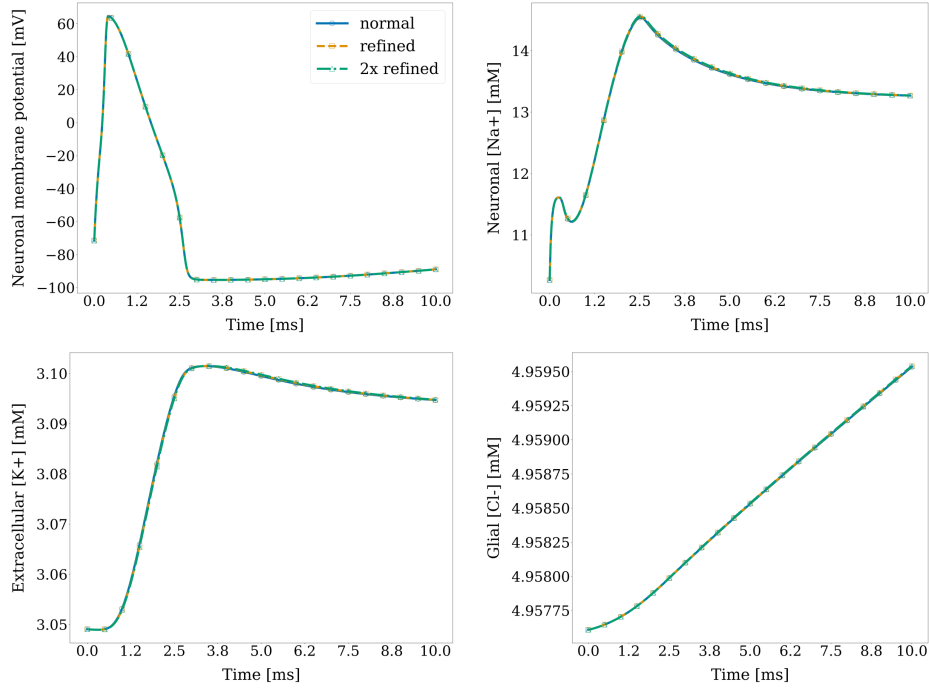


Fig. 14: Convergence of solution under mesh refinement on the $L = 5 \mu\text{m}$, $N = 100$ mouse visual cortex meshes. Three meshes of increasing refinement are considered, and we simulate an action potential as described in Section 5.1. The membrane potential is evaluated on the neuronal membrane at $\mathbf{x} = (1186, 3241, 3594)$ nm, while the concentrations are evaluated in the points described in Figure 8. Common legend for all subfigures.